University of Mississippi

eGrove

1-1-2023

A Study of Electron Energy Response Measurement in the NOvA Test Beam Detector

Devesh Bhattarai
University of Mississippi

Follow this and additional works at: https://egrove.olemiss.edu/etd

A STUDY OF ELECTRON ENERGY RESPONSE MEASUREMENT

IN THE NOvA TEST BEAM DETECTOR

A thesis
presented in partial fulfillment of requirements
for the degree of Master of Science
in the Department of Physics and Astronomy
The University of Mississippi

by

DEVESH BHATTARAI

August 2023

ABSTRACT

The NuMI Off-axis electron-neutrino Appearance (NOvA) experiment at Fermilab is a long-baseline accelerator neutrino experiment designed to study and understand neutrinos through their flavor oscillations between two functionally-identical detectors; a 300-ton Near Detector and a 14 kton Far Detector separated by 809 km and placed 14 mrad off-axis to the Neutrinos at the Main Injector (NuMI) neutrino beam produced at Fermi National Accelerator Laboratory (Fermilab). NOvA has key physics goals to determine the neutrino mass hierarchy, probe CP violation in the leptonic sector, and conduct precise measurements of the neutrino mixing parameters. To help further NOvA's physics reach, the NOvA Test Beam program operates a scaled-down 30-ton detector to measure charged particles found in the final state of neutrino interactions including electrons, muons, pions, kaons, and protons. These particles are identified and momentum-selected within a range of 0.3 to 2.0 GeV/c by a new tertiary beamline deployed at Fermilab. The Test Beam program will provide NOvA with an improved understanding of the largest systematic uncertainties impacting NOvA's oscillation analyses including detector response and detector calibration. This thesis presents the current status of the NOvA Test Beam program and discusses the tagging of electrons and positrons with the beamline data together with preliminary results from detector measurements of their electromagnetic activity and analysis of the electronic properties. Discrepancy seen in the energy variables between data and simulation suggests inaccurate detector calibration. Fake data study of the effect of reduced calibration systematics hints at increased accuracy in the measurement of neutrino oscillation parameters.

DEDICATION

To my parents

Dr. Dhruva Prasad Bhattarai

and

Ms. Bimala Nepal

LIST OF ABBREVIATIONS AND SYMBOLS

HEP	High Energy Physics
CP	Charge Parity
SLAC	Stanford Linear Accelerator Center
PETRA	Positron-Elektron-Tandem-Ring-Anlage
DESY	Deutsches Elektronen-Synchroton
CERN	European Organization for Nuclear Research
CDF	Collider Detector at Fermilab
ATLAS	A Toroidal Large Hadron Collider Apparatus
CMS	Compact Muon Solenoid
LHC	Large Hadron Collider
ILC	International Linear Collider
DUNE	Deep Underground Neutrino Experiment
BSM	Beyond the Standard Model
GUT	Grand Unification Theory
PMNS	Pontercorvo-Maki-Nakagawa-Sakata
NOvA	NuMI Off-Axis Electron Neutrino Appearance
NuMI	Neutrino at the Main Injector
ND	Near Detector
FD	Far Detector
NH	Normal Hierarchy
IH	Inverted Hierarchy
LIGO	Laser Interferometer Gravitational-wave Observatory

VIRGO	Variability of solar IRradiance and Gravity Oscillations
POT	Protons On Target
NC	Neutral Current
CC	Charged Current
LINAC	Linear Accelerator
MI	Main Injector
FHC	Forward Horn Current
RHC	Reverse Horn Current
PVC	Poly Vinyl Chloride
FEB	Front End Board
APD	Avalanche Photo Diode
DCM	Data Concentrator Module
GPS	Global Positioning System
DAQ	Data Acquisition
SNEWS	Supernova Early Warning System
DQ	Data Quality
ADC	Analog-to-Digital Conversion
MIP	Minimum Ionizing Particle
GR	Good Runs
GRL	Good Runs List
TB	Test Beam
MC	Monte Carlo
AD	Accelerator Division
RFQ	Radio Frequency Quadrapole
ToF	Time of Flight
US	Upstream
DS	Downstream

PMT	Photo Multiplier Tube
SiPM	Silicon Photon Multiplier
MWPC	Multi-Wire Proportional Chambers
TDC	Time-to-Digital Controller
TDU	Timing Distribution Unit
u	up quark
d	down quark
s	strange quark
c	charm quark
b	bottom quark
t	top quark
Z^0	neutral Z boson
D^0	neutral D meson
W	W boson
e	electron
p	proton
n	neutron
μ	muon
τ	tauon
ν	neutrino
α	alpha particle
β	beta particle
ν_e	electron neutrino
ν_μ	muon neutrino
ν_τ	tau neutrino
ν_s	sterile neutrino
S	strangeness

$\triangle S$	change in strangeness
I	isospin
ψ	wavefunction
σ	cross section
n_ν	neutrino density
$\bar{\nu}$	antineutrino
$\bar{\nu}_e, \bar{\nu}_\mu, \bar{\nu}_\tau$	electron, muon and tau antineutrino
π	pion
θ	theta
ν_1, ν_2, ν_3	neutrino mass eigenstates
c	speed of light
p	momentum
$\hbar$	Planck's constant
δ	delta
Q	momentum transfer
K	Kaon

ACKNOWLEDGEMENTS

TABLE OF CONTENTS

LIST OF TABLES

CHAPTER 1

INTRODUCTION

1.1 Particle Physics

Particle Physics, also known as High Energy Physics (HEP), is the study of all fundamental particles and forces that make up all matter and radiation in the universe. The fundamental particles in the universe are classified into two basic categories: (i) fermions and (ii) bosons. Fermions are half-odd-integer spin particles that constitute the matter while bosons are force-carrying particles that have integer spins. There are three generations of fermions out of which the first generation consists of up and down quarks responsible for the formation of protons and neutrons. The bosons mediate the three fundamental interactions: electromagnetism, the weak interaction, and the strong interaction. Experimental particle physics deals with the study of these particles produced in particle accelerators or radioactive processes while theoretical particle physics focuses on developing the models, theoretical framework, and mathematical tools needed to understand the experiments and make predictions for future experiments.

1.1.1 History of Particle Physics

The idea that matter is composed of elementary particles dates back to sixth-century B.C.E. The philosophy of atomism was studied by ancient Greek philosophers like Leucippus, Democritus, and Epicurus and Indian philosophers like Kanada, Dignaga, and Dharmakirit. In the medieval period, scientists such as Pierre Gassendi, Robert Boyle, and Issac Newton studied the nature of elementary particles. Alhazen, Avicenna, Gassendi, and Newton proposed the particle theory of light. They proposed that the propagation of light is caused by the rectilinear motion of light particles known as corpuscles. It was believed that these corpuscles travel at a finite speed and

their interactions with the external environment such as rigid surfaces, walls, and the human eye obey Newtonian physics.

In 1802, John Dalton formally stated that everything is made from tiny atoms. Dmitri Mendeleev's first periodic table in 1869 supported the view that matter was actually made of atoms. J.J. Thompson, in the late 1890s, established that electrons are atomic components. Ernest Rutherford, in 1911, showed that atoms have a compact nucleus that contains most of the mass and positive charge of the atom. The nucleus was initially thought to be composed of protons and electrons in order to explain the difference between nuclear charge and mass number but was later found to be composed of protons and neutrons. In the early twentieth century, physicists explored nuclear physics and quantum physics. In 1939, physicist Lise Meitner demonstrated proof of nuclear fission based on the experiments by Otto Hahn. In the same year, proof of nuclear fusion was established by Hans Bethe. The discovery of nuclear fission and nuclear fusion led to the formation of one atom from the other such as the transmutation of a lead atom into a gold atom[1].

In the decades that followed, different varieties of particles were discovered, especially in the 1950s and 1960s. In 1956, a team of physicists led by Frederick Reines and Clyde Cowan observed the evidence of neutrinos by detecting electron antineutrinos produced by a nuclear reactor at the Savannah River plant. In 1963, Murray and Gell-Mann proposed the quark model for the classification of particles. The proposal simplified the situation, which was referred to as the "particle zoo". Important discoveries such as the CP violation by James Cronin and Val Fitch raised a question on matter-antimatter imbalance in the universe[2]. In the early 1970s, the theory of quantum chromodynamics was developed. The theory of quantum chromodynamics described strong nuclear interaction and served as a breeding ground for formulation of the Standard Model, which explained a large number of particles as a combination of a relatively small number of fundamental particles such as leptons and quarks in the realm of quantum field theories leading to the beginning of modern particle physics[3].

Leptons displayed a certain pattern and several papers suggested a fourth quark carrying another flavor to give a similar repeated pattern for the quarks in 1964. Sheldon Glashow and James

Bjorken coined the term charm (c) for the fourth quark. In the following year, O.W. Greenberg, M.Y. Han, and Yoichiro Nambu introduced the quark property of color charge. In 1967, Steven Weinberg and Abdus Salam separately proposed a theory that unified electromagnetic interactions into electroweak interaction. Their theory required the existence of a neutral and weakly interacting boson Z^0. In 1974, John Iliopoulos, while presenting a summary talk for a conference, presented the view of the Standard Model for the first time. Later in 1976, Gerson Goldhaber and Francois Pierre find the D^0 meson, constituted of anti-up and charm quarks. The theoretical predictions agreed dramatically with the experimental results offering support for the Standard Model. In 1976, the tau lepton is discovered by Martin Perl and collaborators at SLAC. This lepton was completely unexpected as it was the first recorded particle of the third generation. In 1977, Leon Lederman and his collaborators at Fermilab discovered another quark and its antiquark, known as the bottom quark (b). This discovery rendered an impetus to physicists to hunt down for the sixth quark - the top quark (t).

In the year that followed, Charles Prescott and Richard Taylor observed a Z^0 mediated weak interaction in the scattering of polarized electrons from deuterium which confirmed a violation of parity conservation as predicted by the Standard Model. In 1979, strong evidence for a gluon radiated by the initial quark or antiquark was found at PETRA, a colliding beam facility at the DESY laboratory in Hamburg. In 1983, the $W^\pm$ and Z^0 intermediate bosons demanded by the electroweak theory are observed by two experiments using the CERN synchrotron, where proton-antiproton collisions incurred. In 1989, experiments carried out in SLAC and CERN strongly suggested that there exists only three generations of fundamental particles by showing that the Z^0-boson lifetime is consistent only with the existence of exactly three light neutrinos. In 1995, the CDF and D0 experiments at Fermilab discovered the top quark at the unexpected mass of 175 GeV but it is not well understood why the mass is so different than the other five quarks. In 2012, the Higgs boson was discovered by the ATLAS and CMS experiments at CERN nearly half a century after Peter Higgs predicted the particle as part of a mechanism by which the fundamental particles gain mass[1,4].

1.1.2 The Future of Particle Physics

Particle physicists worldwide agree upon the most important goals of particle physics research in the near and intermediate future. The goal is to find and understand what physics may lie beyond the Standard Model. There are several experiments to expect new physics, including dark matter and neutrino mass and there are theoretical hints that new physics should be found at accessible energy scales.

Most of the efforts to find new physics are focused on new collider experiments as well as various neutrino experiments. The Large Hadron Collider (LHC), which came into operation in 2008, will continue the search for supersymmetric particles and other new physics. An intermediate goal is the construction of the International Linear Collider (ILC) that will complement the LHC by allowing more precise measurements of the newly found particles' properties. There are also non-collider experiments that attempt to find and understand physics beyond the Standard Model. One important non-collider effort, such as the Deep Underground Neutrino Experiment (DUNE), is to determine the neutrino masses since the masses may arise from neutrinos mixing with very heavy particles. The Snowmass Neutrino Frontier Report[5] presents that the DUNE experiment will fill in the gaps of the three-flavor picture and explore new Beyond the Standard Model (BSM) territory as well as be open to the astrophysical signal opportunities from the skies. The cosmological observations provide many useful constraints on the dark matter, although it may not be possible to determine the exact nature of the dark matter without the colliders. Finally, lower bounds on the very long lifetime of proton put constraints on Grand Unification Theories (GUT) at energy scales much higher than collider experiments, which will be difficult to probe any time soon[1,4].

1.2 The Standard Model of Particle Physics

The Standard Model of particle physics is the theory describing three (excluding gravity) of the four known fundamental forces in the universe and categorizing all known elementary particles[6]. The current formulation was first presented by John Iliopoulos in 1974. Since then, the discovery of the top quark (1995), the tau neutrino (2000), and the Higgs Boson (2012) have

added further support to the theory. In addition to that, the Standard Model has predicted various properties of weak neutral currents and the W and Z bosons with great accuracy. The Standard Model serves as a basis of quantum field theory for the theorists seeking to explain phenomena such as spontaneous symmetry breaking and non-perturbative behavior. It is also the foundation for the formulation of more exotic models that includes hypothetical particles, extra dimensions, and supersymmetry that can explain experimental results not predicted by the Standard Model such as the existence of dark matter and neutrino oscillations (discussed in Section 1.4). Although the theory has exhibited grand success in providing experimental predictions, some of the phenomena remain unexplained. For instance, the theory does not account for baryon asymmetry and does not describe the theory of gravitation. The shortcoming also lies in the theory's inability to explain the universe's accelerating expansion described by the dark energy[7].
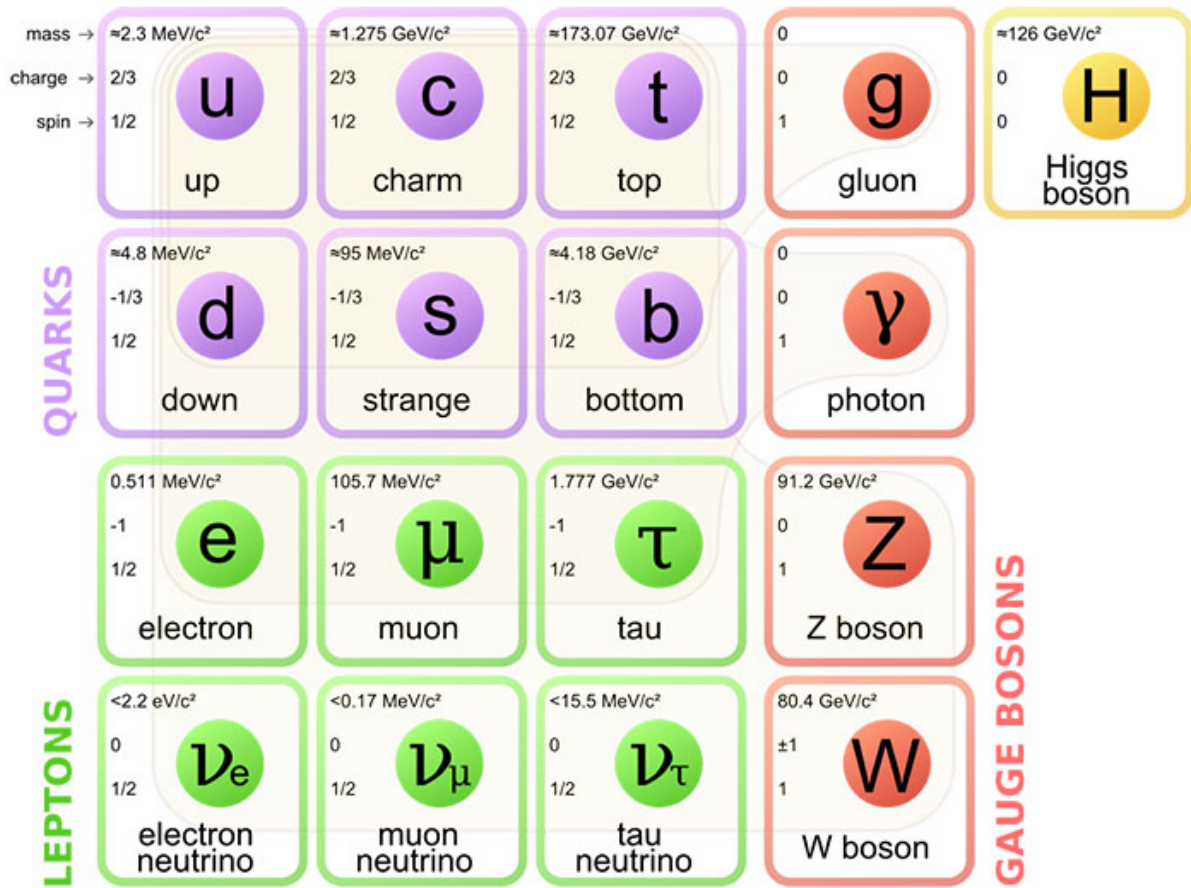
Figure 1.1: The Standard Model describes the elementary particles and forces at the tiny quantum scale.

1.2.1 Leptons and Quarks

According to the Standard Model, all matter is built from a small number of fundamental spin $\frac{1}{2}$ particles or fermions: six quarks and six leptons. The leptons carry an integral electric charge. The electron (e) with a unit negative charge is the most commonly known particle. The other charged leptons are the muon (μ) and the tauon (τ), which are the heavy cousins of the electron. The neutral leptons are called neutrinos (ν). The neutrinos have three different flavors and each flavor is paired with a counter-part charged lepton. For example, in nuclear β-decay, an electron e is emitted together with an electron-type neutrino, ν_e. The charged muon and tauon particles are both unstable and they decay spontaneously to electrons, neutrinos, and other particles. The mean lifetime of the muon is 2.2×10^{-6} s while the mean lifetime of the tauon is only $2.9 \times 10^{-13} \text{s}$ [8].

The quarks carry fractional charges of $+\frac{2}{3}|e|$ or $-\frac{1}{3}|e|$. Just like the leptons, the quarks are grouped into pairs differing by one unit of electric charge. The different quark flavors are: up (u), down (d), strange (s), charm (c), bottom (b), and top (t). The strange quark terminology came into existence as it turned out that it was made up of the so-called strange particles discovered in the cosmic rays long before quarks were even postulated. The strange particles had a peculiar behavior in the sense that they were prolifically produced in strong interactions and they were also expected to decay on a strong interaction timescale of around 10^{-23}s. However, they were observed decaying very slowly via weak interactions. It was theorized that these particles carried a new quantum number, S for strangeness, conserved in strong interactions so that they were always produced in pairs with $S = +1$ and $S = -1$ but they were seen to decay singly and weakly, with a change in strangeness, $\triangle S = \pm 1$, into non-strange particles. On the other hand, the charm quark terminology was a reaction to strangeness while the top quark and the bottom quark terminologies were logically derived for the partners of up and down quarks. The up and down quarks were named because of isospin symmetry, according to which each possesses one of the two components $\pm \frac{1}{2}$ of an isospin vector of value $I = \frac{1}{2}$, which can point up and down like a spin vector.

While leptons can exist as free particles, quarks are confined into a combination. It is due to the presence of strong forces between the quarks that binds them to a combination. The phenomenon

of quark confinement is still not well understood even to this day. Protons and neutrons are made up of the lightest u and d quarks; a proton being a combination of *uud* quarks and a neutron, a combination of *ddu* quarks. Stable particles such as the electrons, the up quark, and the down quark are the most common particles of the present universe. The heavier quarks such as charm, strange, top, and bottom also combine to form particles much heavier than protons and neutrons but those particles are highly unstable and decay rapidly, typically in the order of 10^{-13}s to a combination of up and down quarks. However, these heavy and unstable varieties are observed in very high-energy collisions at particle accelerators or naturally in cosmic rays. The basic properties of leptons and quarks are summarized in Table 1.1.

Particle	Flavour			$Q/|e|$
leptons	e	μ	τ	-1
	ν_e	ν_μ	ν_τ	0
quarks	u	c	t	$+2/3$
	d	s	b	$-1/3$

Table 1.1: General Properties of Leptons and Quarks.

1.2.2 Fermions and Bosons

All of the fundamental particles are categorized into two types: fermions and bosons. Fermions are particles with a half-integral spin that obey Fermi-Dirac statistics. Bosons are particles with an integral spin that obey Bose-Einstein statistics. The statistics obeyed by a particle determines how the wavefunction, ψ, which describes an ensemble of identical particles behaves upon interchanging any pair of particles, for example, particle 1 and 2. However, the probability $|\psi|^2$ cannot be altered by the interchange of $1 \leftrightarrow 2$, since the particles are identical to each other. According to the spin-statistics theorem, a principle of quantum field theory, the following rule holds:

Under the exchange of identical bosons $\psi \rightarrow +\psi$; ψ is symmetric

Under the exchange of identical fermions $\psi \rightarrow -\psi$; ψ is antisymmetric

According to this rule, the wavefunction upon interchanging these two identical particles would not change if nature tries to put two identical fermions in the same quantum state. It is symmetric under the operation. However, this is forbidden by the rule, according to which the wavefunction must change sign. This leads to the famous Pauli's exclusion principle: two or more identical fermions cannot exist in the same quantum state. However, there are no restrictions on the number of bosons in the same quantum state.

An exciting possible extension beyond the Standard Model is the concept of supersymmetry. The theory of supersymmetry predicts a symmetry between fermion and boson at a high energy scale of order 1 TeV. At such an energy scale, each fermion is predicted to have a boson partner and vice versa. The lightest supersymmetric particle is predicted to be stable and electrically neutral. It is also expected to interact weakly with the particles of the Standard Model, which are the characteristics required for dark matter that is thought to make up most of the matter in the universe and hold the galaxies together[8].

1.3   Neutrinos

A neutrino (*Italian: neutral little one*) is an elementary particle with no charge and a very small mass. They are elusive but very abundant particles in the universe. Neutrinos were first proposed in 1930 by Wolfgang Pauli as a desperate remedy to the violation of energy conservation demonstrated by James Chadwick in a continuous spectrum of beta decay when a tritium nucleus undergoes a decay into a helium nucleus and an electron. They are lighter than all the other fermions by several orders of magnitude. Several experimental developments have emerged in the past decade to directly access the neutrino mass scale. Being neutral particles, neutrinos do not feel the electromagnetic interactions. These particles interact only via weak interactions. For example, the cross-section for neutrinos produced in nuclear reactors with energy ~1 MeV is in the order of $\sigma \sim 10^{-44}$ cm^2. The probabilities for such neutrinos to interact in a solid detector with a thickness of one meter and inside the earth traveling along a trajectory passing through its center

are on the order of $\sim 10^{-18}$ and $\sim 10^{-11}$ respectively. The flux of neutrinos produced in the core of the sun through nuclear processes and passing through our body is approximately 60 billion. The neutrino densities inside and outside our bodies are identical. However, the average number density of cosmological neutrinos is $n_\nu \simeq 336$ cm^{-3}. A remarkable number of neutrinos in the order of $\simeq 10^{58}$ is emitted in one supernova explosion triggered by the gravitational collapse of a massive star. Neutrinos emerging from deep inside the core of astrophysical objects reveal directly the physical processes operating there making them precious messengers from distant objects.

Neutrinos can interact via two processes: neutral current interactions and charged current interactions as shown in Figure 1.2. In neutral current interactions, neutrinos couple with a Z^0 boson keeping their identity and changing their 4-momentum. However, in charged current interactions, they can couple with a $W^\pm$ boson and transform into one of the charged leptons: $e^\pm, \mu^\pm$ or $\tau^\pm$. The charged current interaction leads to the concept of neutrino flavor. The flavor of a neutrino is defined as the type of charged lepton that is connected to the same charged current vertex. Different vertices can generate different types of processes. Let us consider the example of the decay of a virtual W^- or W^+:

$$W^+ \rightarrow l^+ + \nu_l, \qquad W^- \rightarrow l^- + \bar{\nu}_l$$

where the label $l = e, \mu, \tau$ of the neutrino corresponds to the mass or type of the charged lepton known as the neutrino flavor and $\bar{\nu}_l$ represents an antineutrino of the corresponding lepton flavor.
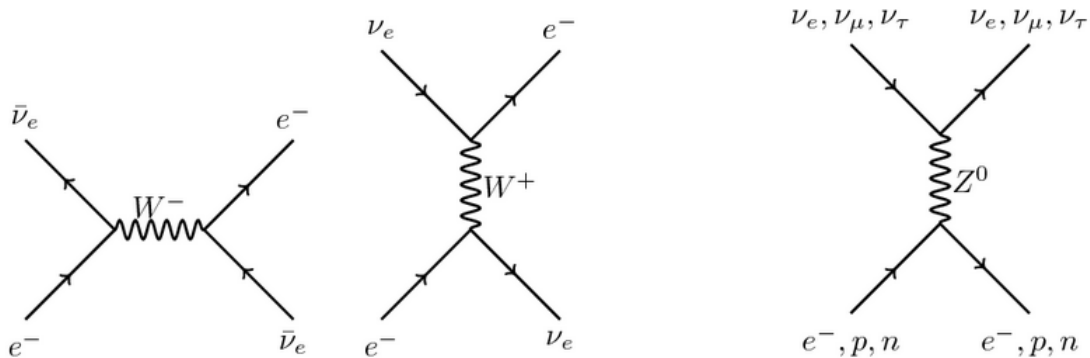
Figure 1.2: The Feynman diagrams for charged current interactions (left and middle) and neutral current interaction (right).

Neutrinos are half interger spin particles. In the 1950s, it was found that all neutrinos have their spin anti-parallel to their momentum while all the antineutrinos have their spin parallel to their momentum as shown in Figure 1.3. In short, all the neutrinos are left-handed particles while all the antineutrinos are right-handed. This is the source of parity violation as observed in nature. This information also leads to a possibility that a neutrino and antineutrinos are just two different spin states of a two-state Majorana particle which implies the neutrino is an antiparticle of itself. This is different from the other Dirac particles having 4 states: particle and antiparticle each with two independent spin states.
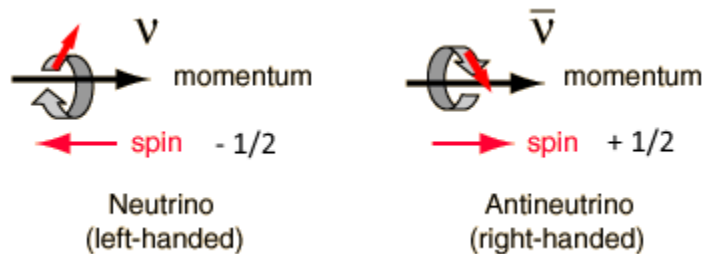
Figure 1.3: A diagram showing the directions of spin and momentum of a neutrino and an antineutrino. In the case of neutrinos, the spin opposes the momentum while they are in the same direction in the case of an antineutrino.

Neutrinos originate from different sources in the universe. Cosmological neutrinos are the leftover neutrinos from the early epochs of the evolution of the universe. The number density of cosmological neutrinos is ~ 56 cm^{-3} for each neutrino species. These neutrinos have a black-body spectrum with a temperature $\simeq 1.947$ Kelvins. In a supernova explosion, almost all (99%) of the energy is radiated away in the form of neutrinos as shown in the process:

$$e^- + p \rightarrow n \rightarrow \bar{\nu}_e$$
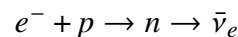
It is likely the neutrinos emitted by the proto neutron star play a crucial role in the explosion. Neutrinos emitted in a supernova explosion were observed in 1987 when the neutrinos and the radiation of a supernova (SN1987A) that exploded 170,000 years before in the Large Magellanic Cloud reached the Earth. Through the process of nuclear reactions, neutrinos are also produced in the stars. For example, protons and electrons combine to form a helium atom in the sun liberating

energy and the neutrinos with a flux of approximately 6×10^{10} cm^{-2} s^{-1} in the process:

$$4p + 2e^- \rightarrow {}^4\text{He} + 2\nu_e + 26.73 \text{ MeV}$$
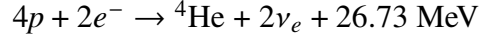
The detailed spectrum of the emitted neutrinos depends on the path taken by the nuclear reactions to burn hydrogen into helium. A prominent source of neutrinos is the natural radioactivity. As the earth emits approximately 40 TW of energy, about 40% of this energy is due to the decay of radioactive nuclei. About 90% of the decay is due to decay chains due to the Uranium and Thorium decay chains. A cascade of 8 α and 6 β transitions that terminate in the stable nucleus ^{206}Pb is initiated by ^{238}U nucleus. Similarly, a cascade of 6 α and 4 β transitions that terminates in ^{208}Pb nucleus is initiated by ^{238}Th nucleus. In each of β decay, a $\bar{\nu}_e$ is emitted with a maximum energy of 3.27 MeV. The decays take place at the surface of the Earth with a flux in the order of $\sim 10^6$ (cm^2 s)$^{-1}$. Another source of neutrino is the atmosphere. The Earth's atmosphere receives an approximately isotropic and constant flux of cosmic rays with an intensity of 0.5 particles/cm^2. The primary cosmic rays that interact in the upper atmosphere generate a number of secondary particles such as pions and kaons. These particles produce neutrinos through the decay in the following processes:

$$\pi^+ \rightarrow \mu^+ + \nu_\mu, \qquad \mu^+ \rightarrow e^+ + \nu_e + \bar{\nu}_\mu$$

Apart from these natural sources, there are two important artificial sources of neutrinos: reactor neutrinos and accelerator neutrinos[9]. In the past decades, four nobel prizes have been awarded in the field of neutrino physics: F. Reines (1995) for the discovery of neutrinos; L. Lederman, J. Steinberger and M. Schwartz (1988) for the discovery of muon neutrinos; R. Davis and M. Koshiba (2002) for the detection of cosmic neutrinos and A. McDonalnd and T. Kajita (2015) for the discovery of neutrino oscillations.

1.4 Neutrino Oscillations

Neutrino oscillation is a remarkable Quantum Mechanical phenomenon where the probability of finding a neutrino created in one flavor state to be in the same state or any other flavor

state can oscillate with time. The idea of the possible existence of neutrino oscillations was first introduced by Bruno Pontecorvo. It was later observed in 1998 by the Super-Kamiokande experiment establishing that neutrinos have non-zero and non-degenerate masses. As it is practically impossible to measure the mass of a neutrino, the amplitudes for the production of neutrinos with different masses must be coherently added. These amplitudes of different mass components evolve differently with space and time. Different quantum mechanical phases are acquired implying that the flavor is a periodical function of time. If the neutrino masses are close to each other, a longer time is required to have an appreciable phase difference between the different components. The neutrinos travel at approximately the speed of light due to which a transition to a different flavor becomes significantly different from zero only for a long distance between the production and detection points. Longer path length also allows the measurement of tiny mass differences between the neutrinos [9].

1.4.1 Theoretical Background for Neutrino Oscillation

As mentioned in the previous section, neutrinos come in three different flavors: ν_μ, ν_e, and ν_τ. The subscripts denote the type of interactions these neutrinos mostly undergo. These neutrinos are also the eigenstates of a Hamiltonian that governs their interactions. The neutrino interaction is not limited to their denoted subscripts but in fact, they do have other types of interactions in which the energy eigenvalues for the interactions relate to the states with well-defined masses that can be written as ν_1, ν_2 and ν_3. The interaction of neutrinos with these states means that one could expand ν_μ, ν_e and ν_τ according to ν_1, ν_2 and ν_3. For example, if we only consider ν_μ and ν_e, we can write:

$$|\nu_e\rangle = -\sin\theta\,|\nu_1\rangle + \cos\theta\,|\nu_2\rangle\,, \quad |\nu_\mu\rangle = \cos\theta\,|\nu_1\rangle + \sin\theta\,|\nu_2\rangle \tag{1.1}$$

The above-mentioned expressions have θ as a representation of a mixing angle that shows up in a unitary transformation connecting the flavor of neutrinos to the mass neutrinos. There is no specific value set for these angles and the phenomenon by which one could measure these mixing angles is neutrino oscillations.

As time evolves, phase differences will appear. Let us consider at $t = 0$, the eigenstate of the neutrino is $|\nu_e\rangle$. Due to the difference in the masses of ν_1 and ν_2, each will evolve with a different frequency and this would cause a relative phase difference. One can measure these evolving phase differences and oscillations with a period that depends on the difference between the masses of ν_1 and ν_2. To measure the different parameters of neutrino oscillation, it is useful to remind oneself that the neutrinos are ultra-relativistic and hence their energy will be obtained from the following relation[10]:

$$E = \sqrt{(pc)^2 + (mc^2)^2} \simeq pc(1 + \frac{(mc)^2}{2p^2})$$ (1.2)

In light of neutrino flavor oscillations, Pontecorvo and others questioned the masslessness of the neutrinos, and the mathematical evaluation was developed by Ziro Maki, Masami Nakagawa, and Soichi Sakata[11]. It was proposed that while neutrinos are created or annihilated as flavor eigenstates, they propagate through space as a superposition of mass eigenstates. The weak interaction eigenstates ν_μ, ν_e and ν_τ are therefore expressed as combinations of mass eigenstates ν_1, ν_2 and ν_3 that propagate with slightly different frequencies due to their different masses and between which different phases develop with distance traveled, corresponding to a change in the neutrino flavor[8]. The flavor basis ν_μ, ν_e and ν_τ and the mass basis ν_1, ν_2 and ν_3 are related by a unitary transformation of the form:

$$|\nu_\alpha\rangle = \sum_i U^*_{\alpha i} |\nu_i\rangle$$ (1.3)

where $\alpha = e, \mu, \tau$ is the neutrino flavor and $i = 1, 2, 3$ is related to the mass eigenstates. This relation can also be written as:

$$|\nu_i\rangle = \sum_\alpha U_{\alpha i} |\nu_i\rangle$$ (1.4)

where U is known as the Pontercorvo-Maki-Nakagawa-Sakata (PMNS) mixing matrix[12,13]. In order to simplify the treatment, we consider the case of two neutrino flavors, ν_e and ν_μ. Each will be a linear combination of two mass eigenstates, ν_1 and ν_2 given by the unitary transformation

involving an arbitrary mixing angle θ:

$$\begin{bmatrix} v_\mu \\ v_e \end{bmatrix} = \begin{bmatrix} \cos\theta & \sin\theta \\ -\sin\theta & \cos\theta \end{bmatrix} \begin{bmatrix} v_1 \\ v_2 \end{bmatrix} \tag{1.5}$$

The wavefunctions $|v_e\rangle = -\sin\theta \, |v_1\rangle + \cos\theta \, |v_2\rangle$ and $|v_\mu\rangle = \cos\theta \, |v_1\rangle + \sin\theta \, |v_2\rangle$ are orthonormal states. Thus, the propagation in space is given by:

$$v_1(t) = v_1(0)e^{-itE_1} \tag{1.6}$$

$$v_2(t) = v_2(0)e^{-itE_2} \tag{1.7}$$

where $h = c = 1$. The stats v_1 and v_2 will have a fixed momentum p, so that if the masses are $m_i << E_i$ (where $i = 1, 2$).

$$E_i = p + \frac{m_i^2}{2p} \tag{1.8}$$

If we were to start off at $t = 0$ with a muon neutrinos, then $v_\mu(0) = 1$ and $v_e(0) = 0$. Inverting the unitary transformation leads to the following:

$$v_1(0) = v_\mu(0)\cos\theta \tag{1.9}$$

$$v_2(0) = v_\mu(0)\sin\theta \tag{1.10}$$

$$v_\mu(t) = \cos\theta v_1(t) + \sin\theta v_2(t) \tag{1.11}$$

We therefore obtain the amplitude:

$$A_\mu = \frac{v_\mu(t)}{v_\mu(0)} = \cos^2(\theta)e^{-itE_1} + \sin^2(\theta)e^{-itE_2} \tag{1.12}$$

14

The intensity can be written as:

$$\frac{I_\mu(t)}{I_0(t)} = A_\mu A_\mu^* = 1 - \sin^2(2\theta)\sin^2(\frac{(E_2 - E_1 t)}{2}) \tag{1.13}$$

Writing $\Delta m^2 = m_1^2 - m_2^2$ and using the energy equation, we obtain the following form for the probability of finding ν_μ or ν_e after $t = L/c$, where L is the distance travelled:

$$P(\nu_\mu \to \nu_\mu) = 1 - \sin^2(2\theta)\sin^2(\frac{1.27\Delta m^2 L}{E}) \tag{1.14}$$

$$P(\nu_\mu \to \nu_e) = 1 - P(\nu_\mu \to \nu_\mu) \tag{1.15}$$

The numerical constant is obtained by retaining the h, c terms that are set to unity. The phase angle then becomes $\Delta m^2 c^4 L/(4E\hbar c)$ so that expressing L in meters, $(\Delta mc^2)^2$ in $(eV)^2$ and E in MeV with $\hbar c = 197$ MeVfm, the constant 1.27 follows. The equation shows that the neutrino flavor oscillates with the time or distance traveled by the beam. The diagram below shows the oscillation for $\theta = 45°$:
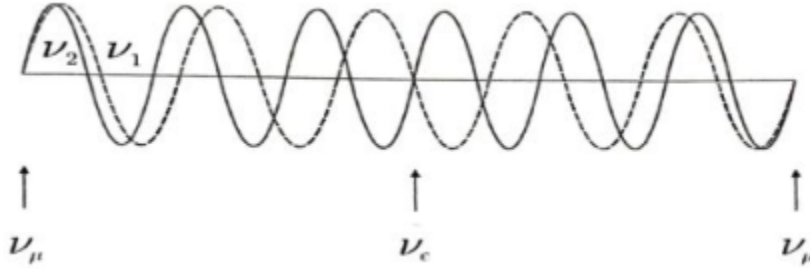
Figure 1.4: A diagram showing a two-neutrino oscillation scenario, showing the amplitude of ν_1 and ν_2 mass eigenstates for $\theta = 45°$. The two are in phase at the beginning and the end of the plot, separated by one oscillatory wavelength. These are pure ν_μ flavor eigenstates. The two amplitudes are 180° out of phase in the center of the plot corresponding to the ν_e weak eigenstate.

It can be seen that as it traverses the space, the beam initially starting off as ν_μ oscillates back and forth between a pure ν_μ and a pure ν_e eigenstate as shown in Figure 1.4. For other values of θ, the beam will oscillate between a pure ν_μ eigenstate and a superposition of ν_e and ν_μ. For the case of

3-neutrinos, the mixing between the flavor and the mass states can be expressed as:

$$
\begin{bmatrix} \nu_e \\ \nu_\mu \\ \nu_\tau \end{bmatrix} = \begin{bmatrix} U_{e1} & U_{e2} & U_{e3} \\ U_{\mu 1} & U_{\mu 2} & U_{\mu 3} \\ U_{\tau 1} & U_{\tau 2} & U_{\tau 3} \end{bmatrix} \begin{bmatrix} \nu_1 \\ \nu_2 \\ \nu_3 \end{bmatrix}
\tag{1.16}
$$

where the mixing matrix U is parameterized[14] as $U = R_{23}S_{13}R_{12}$, where textitR$_{ij}$(S_{ij}) is a real (complex) rotation by an angle θ_{ij} in the ij plane.

$$
U = R_{23}S_{13}R_{12} = \begin{bmatrix} 1 & 0 & 0 \\ 0 & c_{23} & s_{23} \\ 0 & -s_{23} & c_{23} \end{bmatrix} \begin{bmatrix} c_{13} & 0 & s_{13}e^{-i\delta} \\ 0 & 1 & 0 \\ -s_{13}e^{i\delta} & 0 & c_{13} \end{bmatrix} \begin{bmatrix} c_{12} & s_{12} & 0 \\ -s_{12} & c_{12} & 0 \\ 0 & 0 & 1 \end{bmatrix}
\tag{1.17}
$$

$$
U = \begin{bmatrix} c_{12}c_{13} & s_{12}c_{13} & s_{13}e^{-i\delta_{CP}} \\ -s_{12}c_{23} - c_{12}s_{23}s_{13}e^{i\delta_{CP}} & c_{12}c_{23} - s_{12}s_{23}s_{13}e^{i\delta_{CP}} & s_{23}c_{13} \\ s_{12}s_{23} - c_{12}c_{23}s_{13}e^{i\delta_{CP}} & -c_{12}s_{23} - s_{12}c_{23}s_{13}e^{i\delta_{CP}} & c_{23}c_{13} \end{bmatrix}
\tag{1.18}
$$

where $c_{ij} = cos(\theta_{ij})$, $s_{ij} = sin(\theta_{ij})$ and $\delta = \delta_{CP}$ is the Dirac phase that allows Charge-Parity (CP) violation in the lepton sector. If δ_{CP} is found to be a non-integer (i.e. $\delta_{CP} \neq 0, \pi, 2\pi$), it states that the neutrinos and antineutrinos would oscillate differently[15]. This parameterization leads to $\frac{N(N-1)}{2}$ mixing angles and $\frac{(N-1)(N-2)}{2}$ phases for a total of $(N-1)$ parameters[12,13].

CHAPTER 2

THE NOvA EXPERIMENT

2.1   Introduction to the NOvA Experiment

The NOvA (acronym for the NuMI Off-axis Electron-neutrino Appearance) experiment is a long baseline neutrino oscillation experiment hosted by Fermi National Accelerator Laboratory (Fermilab). The experiment focuses on the measurement of neutrino and antineutrino oscillation in two disappearance channels ($\nu_\mu \rightarrow \nu_\mu$, $\bar{\nu}_\mu \rightarrow \bar{\nu}_\mu$) and two appearance channels ($\nu_\mu \rightarrow \nu_e$, $\bar{\nu}_\mu \rightarrow \bar{\nu}_e$). NOvA uses the NuMI (acronym for Neutrinos at Main Injector) beam, a high intensity beam that primarily contains muon anti-neutrinos, delivered by the Fermilab Accelerator Complex. The experiment consists of two functionally identical detectors stationed 809 km apart. The Near Detector (ND) is placed under the ground surface at 1 km away from the NuMI target in Fermilab while the Far Detector (FD) is placed on the Earth's surface in Ash River, Minnesota as shown in Figure 2.1. The experiment uses data from the Near Detector and predicts the event spectrum visible at the Far Detector. The energy spectra of ν_μ and ν_e events are measured in the Far Detector after the neutrinos undergo the oscillation process and they are compared to the expected spectra for various values of the mixing parameters in order to determine the neutrino mixing parameters.
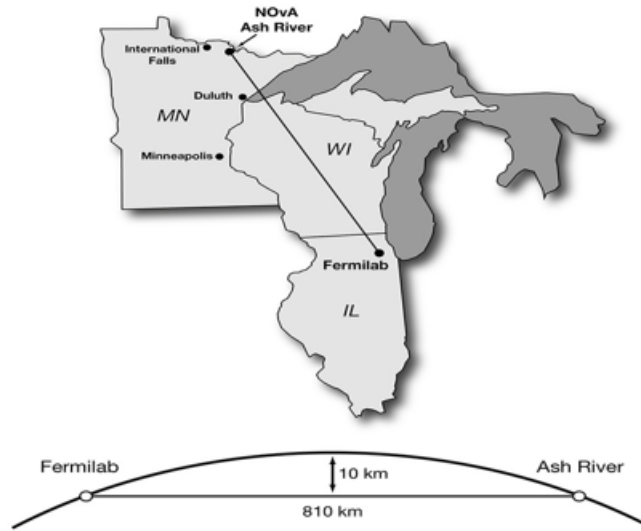
Figure 2.1: A diagram showing an overview of the NOvA Experiment. The NuMI beam and Near Detector are in Fermilab while the Far Detector is in Ash River, Minnesota.

2.2 Objectives of the NOvA Experiment

The NOvA experiment is primarily designed to answer some of the fundamental questions in neutrino physics. The objectives of the NOvA experiment can be summarized as follows:

2.2.1 Oscillation of Antimuon Neutrinos to Antielectron Neutrinos

Neutrinos oscillate between the three flavors. Physicists have observed the oscillation of muon neutrinos to tau neutrinos and electron neutrinos. What has not been observed is the oscillation of antimuon neutrinos to antielectron neutrinos. Several unknown factors that govern neutrino oscillation are yet to be known. The NOvA experiment looks for the signals if the neutrinos are oscillating from antimuon flavor to antielectron flavor on their 810 km journey from Fermilab, IL to Ash River, MN.

2.2.2 Ordering of the Neutrino Masses

Neutrinos are the lightest elementary particles. However, neither the mass of each neutrino flavor nor the mass hierarchy is known. Physicists believe that neutrinos get their masses through a different process than other particles. Making a neutrino of a particular mass requires a combination

18

of three flavors. The first type is mostly the electron flavor. The second type uses roughly equal amounts of electron, muon, and tau while the third is nearly an equal mixture of muon and tau. The Normal Hierarchy (NH) predicts the neutrino mass eigenstates in the order $v_3 > v_2 > v_1$ making v_e a lighter particle while the Inverted Hierarchy (IH) predicts the neutrino mass eigenstates in the order $v_2 > v_1 > v_3$ making v_e a heavier particle. The mass hierarchy is also important to know if neutrinos are their own antiparticles. The NOvA Experiment hopes to determine the mass hierarchy by comparing oscillations of a beam of muon neutrinos and muon antineutrinos.

2.2.3 Symmetry between Matter and Antimatter

Matter and antimatter were created in equal amounts during the big bang. When they interact with one another, they are both erased from existence as they annihilate each other. If so, how do the matter particles in our universe dominate over the antimatter particles? Physicists believe that at one point matter and antimatter behaved differently and they are not exactly the mirror images of one another. This hints at Charge-Parity (CP) violation. The NOvA Experiment uses the NuMI beam and the neutrino detectors to study the neutrino and antineutrino oscillations. If antineutrinos and neutrinos do not follow the same pattern when they change from one flavor to another, this indicates CP violation. The same process that caused antineutrino oscillations and neutrino oscillations to be different could have led to the dominance of matter over antimatter in the early stage of the universe.

Besides addressing the pressing questions in neutrino physics, the NOvA experiment is also capable to look for some of the exotic phenomena such as sterile neutrinos, magnetic monopoles and energetic showers while also making precision measurements of neutrino cross-section. The NOvA Far Detector searches for the lows-mass magnetic monopoles and monitors the flux of the highly energetic cosmic ray showers. Searches for the sterile neutrinos are also done in the Far Detector. The Near Detector is capable of looking for the presence of possible elusive Dark Matter particles in the high-intensity NuMI neutrino beam and studying the seasonal variations of multi-muon cosmic flux components. Neutrino cross-section measurements are also performed in the

Near Detector. Both detectors in combination serve as a powerful supernova neutrino detector and also allow for the multi-messenger signal searches in coincidence with LIGO/VIRGO[16].

2.3 Latest Publications by the NOvA Experiment

The NOvA experiment is built to precisely measure the neutrino mixing parameters, probe CP violation in the lepton sector and determine the neutrino mass hierarchy and has been collecting data since February 2014. As of February 2023, NOvA has a total of 26 publications, out of which 7 have been published in Physical Review Letters (PRL) and 11 in Physical Review D (PRD). In this section, some of the findings from the latest three-flavour results is discussed.

In August 2022, NOvA published results on the improved measurement of neutrino oscillation parameters through $\nu_\mu \to \nu_e$, $\nu_\mu \to \nu_\mu$, $\bar{\nu}_\mu \to \bar{\nu}_e$ and $\bar{\nu}_\mu \to \bar{\nu}_\mu$ oscillation modes. It was a 50% increase in neutrino-mode beam exposure over the previously reported results. The additional data was combined with previously published neutrino and antineutrino data and were all analyzed using improved techniques and simulations. A joint fit to the ν_e, ν_μ, $\bar{\nu}_e$ and $\bar{\nu}_\mu$ candidate samples within the 3-flavor neutrino oscillation framework continued to yied the best-fit point in the normal mass ordering and the upper octant of the θ_{23} mixing angle, with $\Delta m^2_{32} = (2.41 \pm 0.07) \times 10^{-3}$ eV^2 and $\sin^2(\theta_{23}) = 0.57^{+0.03}_{-0.04}$. The data disfavored combinations of oscillation parameters that gave rise to a large asymmetry in the rates of ν_e and $\bar{\nu}_e$ appearance which included values of the CP-violating phase in the vicinity of $\delta_{CP} = \pi/2$ exluded by 3σ for the inverted mass ordering and values around $\delta_{CP} = 3\pi/2$ in the normal ordering disfavored at 2σ conifdence[17].

2.4 The NuMI Beam

The NuMI (acronym for the Neutrinos at the Main Injector) beam consists of the neutrinos for the NOvA experiment and is created by firing protons from Fermilab's Main Injector into a graphite target. These protons are obtained from H$^-$ ion source when accelerated to 400 MeV in LINAC (Linear Accelerator) and subsequently in a booster ring up to 8 GeV. These protons are then passed to a recycler ring in two batches while maintaining the energy at 8 GeV. The recycler

has the same circumference as the Main Injector ring of 3.3 km (Figure 2.2) and can accommodate six of these two batches as it is much bigger than the booster. The beam intensity is thus increased by combining two batches into a single Main Injector (MI) ring. The set of six proton beam batches together is called a spill and each NuMI beam spill is 10 μs long. The protons are further accelerated up to 120 GeV. NuMI beam initially started with a power of 400 kW. Upgrades have been performed to make it the most powerful neutrino beam in the world with a power of 700 kW[18]. However, NuMI beam has recorded the highest power ever at 950 kW.
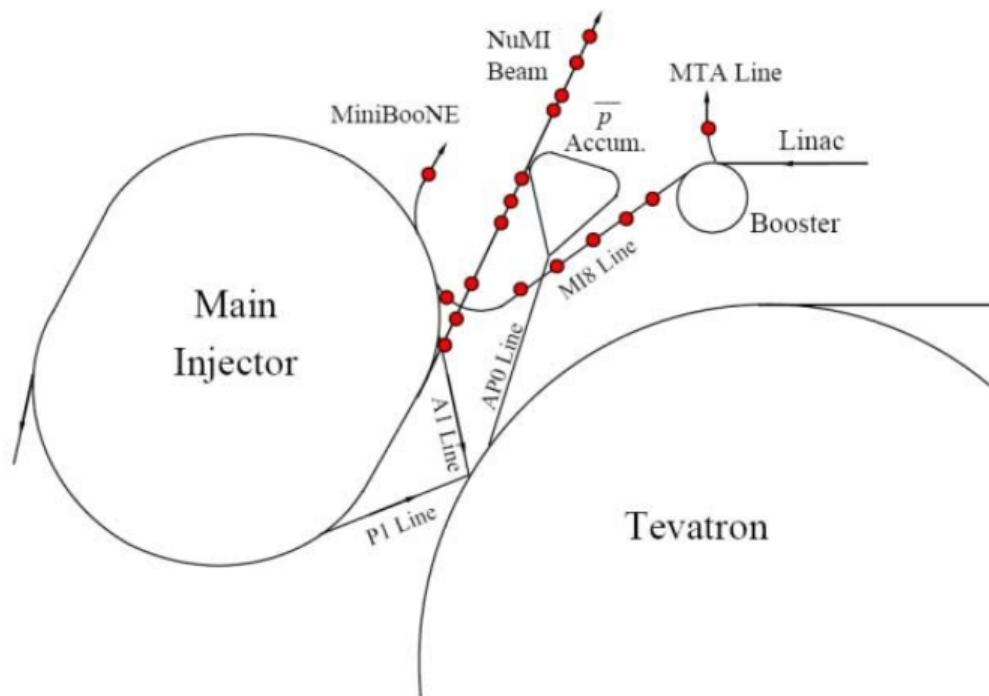
Figure 2.2: Schematic diagram of a portion of the Fermilab accelerator complex including the beam lines for NuMI.

Upon collision of 120 GeV protons on a graphite target, various fundamental particles come out including charged particles like the pions and kaons. The pions and kaons are steered with the help of magnetic focusing horns in a direction where the neutrinos are intended to travel and the charge of pions and kaons (positive/negative) determines neutrino/antineutrino mode. The two modes of beam operation are called the Forward Horn Current (FHC) and Reverse Horn Current (RHC). The pions undergo a decay process in a 675 m long decay pipe (shown in Figure 2.3) filled
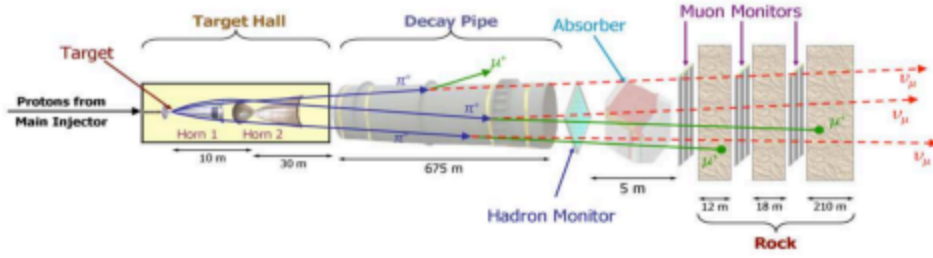
Figure 2.3: Components of the NuMI beam.

with helium to minimize interactions prior to decay.

The primary source of neutrinos in the NuMI beamline are pion decays and kaon decays governed by the following process:

$$\pi^+ \rightarrow \mu^+ + \nu_\mu$$

$$K^+ \rightarrow \mu^+ + \nu_\mu$$

$$\pi^- \rightarrow \mu^- + \bar{\nu}_\mu$$

$$K^- \rightarrow \mu^- + \bar{\nu}_\mu$$
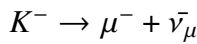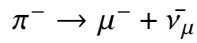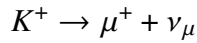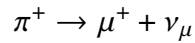
The hadrons then go through a hadronic monitor and are absorbed by the concrete absorber downstream of the decay pipe as shown in Figure 2.3. The decay of kaons also generates ν_e which leads to the presence of ν_e background in the beam. The particles later go through the muon shield where any remaining muons are removed from the beam before reaching the Near Detector clearing the path for muon neutrinos. A small portion of contamination also comes from wrong sign neutrinos such as neutrinos in antineutrino dominant beam mode and antineutrinos in neutrino dominant beam mode coming from wrong sign hadrons due to π^- for neutrino dominant beam mode and π^+ for antineutrino dominant beam mode[19]. The NuMI beam is then aimed $3.3°$ downwards. Although the beam begins 150 feet below the ground at Fermilab, it will pass as much as six miles below the surface as it travels toward Ash River. The beam gradually spreads apart as it travels, the width being about six feet at Fermilab but growing to several miles by the time it reaches the Far Detector.

2.5   NOvA Detectors

The NOvA experiment consists of two main detectors that are functionally identical. The Near Detector (Figure 2.5) weighs 300 metric-ton and is located in Fermilab. It is designed to measure the unoscillated beam spectra so that it can be used to predict the Far Detector spectrum. It is placed 100 m under the ground surface and lies at a distance of around 1 km from the NuMI target. The dimensions of the Near Detector read 3.9 m × 3.9 m × 15.9 m. It consists of 20000 cells of extruded and highly reflective Poly Vinyl Chloride (PVC) plastic filled with liquid scintillator collectively known as the channels. The 14 kton Far Detector (Figure 2.4) is much larger in size than the Near Detector. It is placed on the surface in Ash River, Minnesota at a distance of 810 km from the target. The dimensions of the Far Detector read 15 m × 15 m × 60 m. The Far Detector consists of 344000 channels.
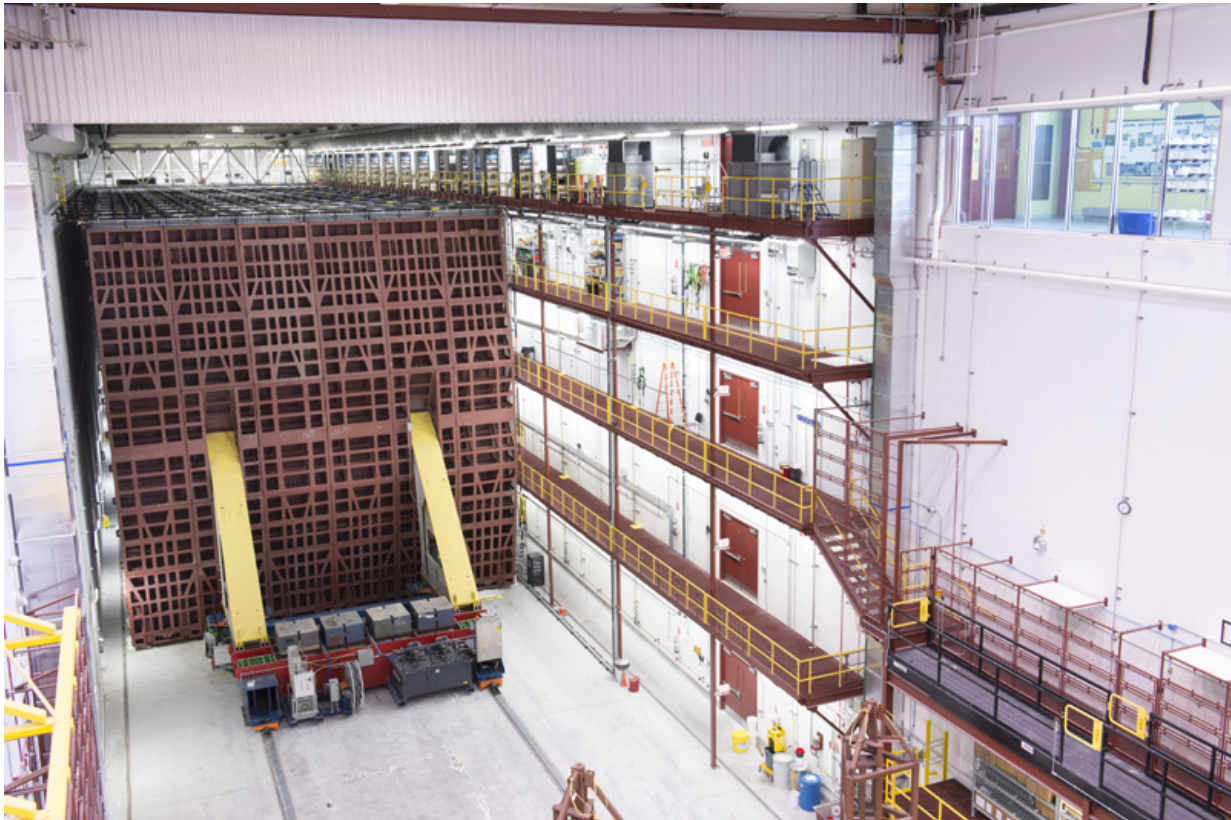
Figure 2.4: A picture of NOvA Far Detector located in Ash River.
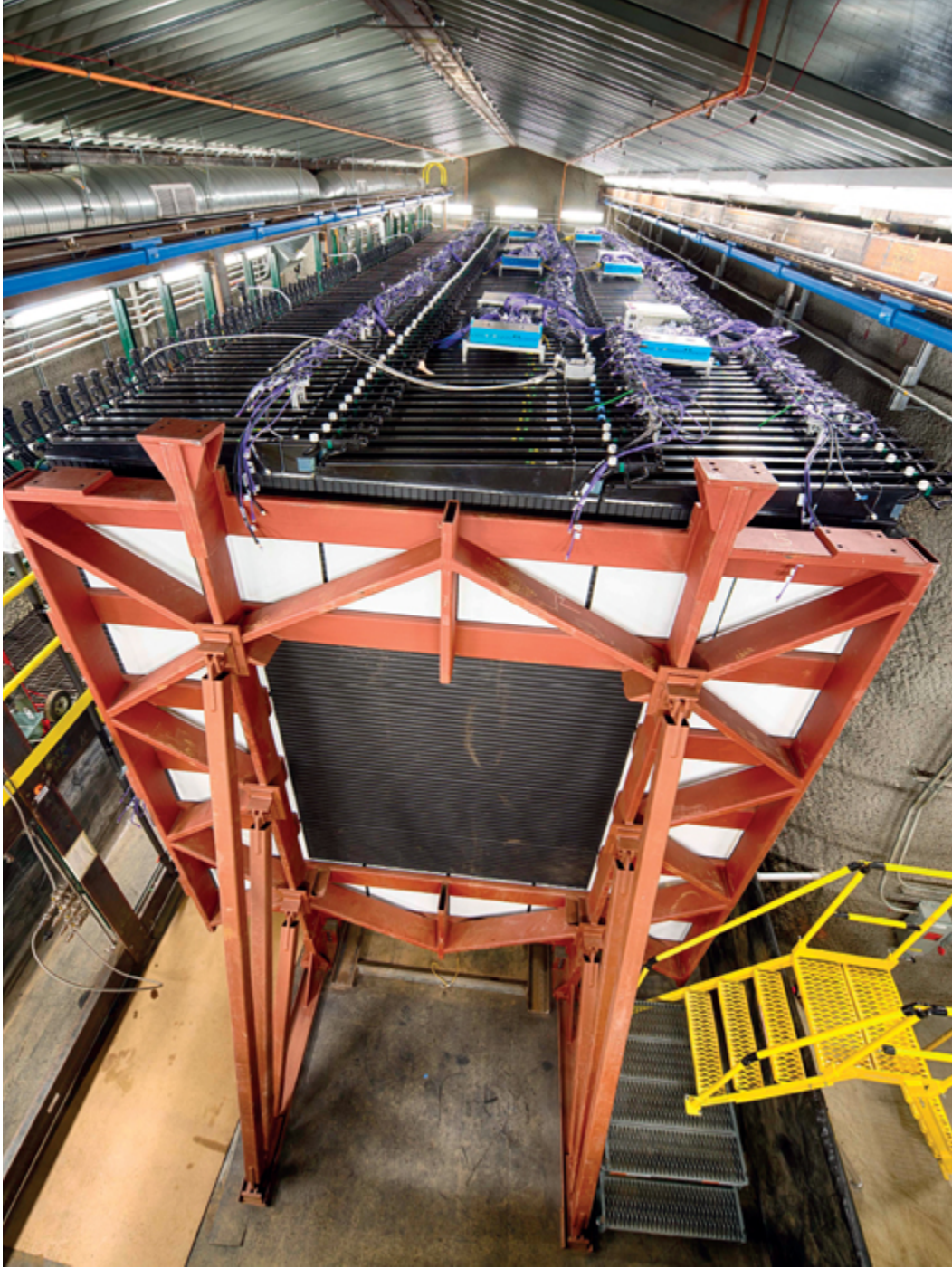
Figure 2.5: A picture of NOvA Near Detector located in Fermilab.

Each detector is filled with a liquid scintillator that accounts for 63% of the active detector material. The liquid scintillator is a mixture of different chemical components but predominantly contains mineral oil solvent. Both detectors have the same basic unit known as the cell. The cells

constitute 37% of the detector material. Each cell measures 3.5 cm $\times$ 5.6 cm $\times$ the length of the detector. The wall of each cell has a thickness in the range of 2 - 4.5 mm. Each cell is a pure PVC compounded with titanium oxide and other ingredients to form a powder that can be melted into the desired plastic shape. The interior of a cell is highly reflective to allow the reflection and passage of light through the wavelength-shifting fiber (Figure 2.6). The wavelength-shifting fiber is an optical fiber of 0.7 mm diameter placed inside of each cell. Whenever a particle passes through a cell and deposits energy on the liquid scintillator after recording a hit on the highly reflective walls, the blue light is shifted to the green spectrum.
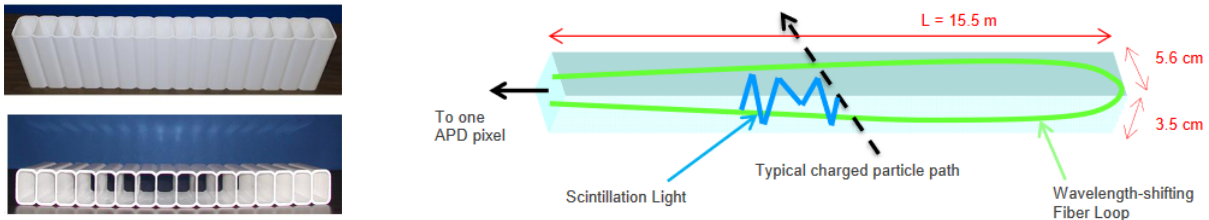
Figure 2.6: A picture of NOvA Cell (left) and wavelength shifting fiber (right).

Information about all of the particles passing through the detector is in the form of light. Various electronic instruments convert the light into a format in which the data can be analyzed. The Front End Board (FEB) has an Avalanche Photo Diode (APD) (Figure 2.7) that converts light to electricity through a photoelectric effect. The FEBs are basically electronic circuit boards positioned towards the end of a cell and are responsible for digitizing the analog signals from APD. The data from each FEB is collected in a DCM (Data Concentrator Module). A DCM issues timing information to each FEB and passes the data to the processing farm where pixel images of the deposited charge are analyzed to reconstruct energy and classify neutrino interactions.

Figure 2.7: A picture of APD (left) where the ends of 32 wavelength-shifting fibers are collected at the end of scintillation cells, FEB (middle) and DCM (right).

As the two detectors are huge in size, a well-designed timing system is in place to coordinate and time stamp the data within each section of the detector. It works through coordination with Near Detector, Far Detector, and beam spill timing. Global Positioning System (GPS) is used to track the NuMI neutrino beam which gives us information at exactly what time the beam arrived. The NOvA Data Acquisition (DAQ) system collects all the data by recording different events. Some of the events are beam neutrino events caused by the NuMI beam from Fermilab. Both detectors record 550 μs of data each time they receive a NuMI trigger. Calibration data events are used to calibrate the Far Detector while an activity-based trigger is used to calibrate the Near Detector. The detectors are also equipped with external triggers capable of finding supernova events through the Supernova Early Warning System (SNEWS) or the magnetic monopole events.

The NOvA detectors are placed 14.6 mrad off the NuMI beam axis. As the pions and kaons are not decaying at rest, the energy spectrum of resulting neutrinos is not uniform and depends on the angle between the direction of boost and the direction of neutrino production. The first oscillation maximum occurs around 2 GeV for NOvA's baseline of 810 km. At this angle, a larger amount of neutrinos is seen at 2 GeV than if it were to be on the beam axis as shown in Figure 2.8. Having the detectors placed off-axis also has a benefit of decreased Neutral Current (NC) background events which can mimic ν_e events.
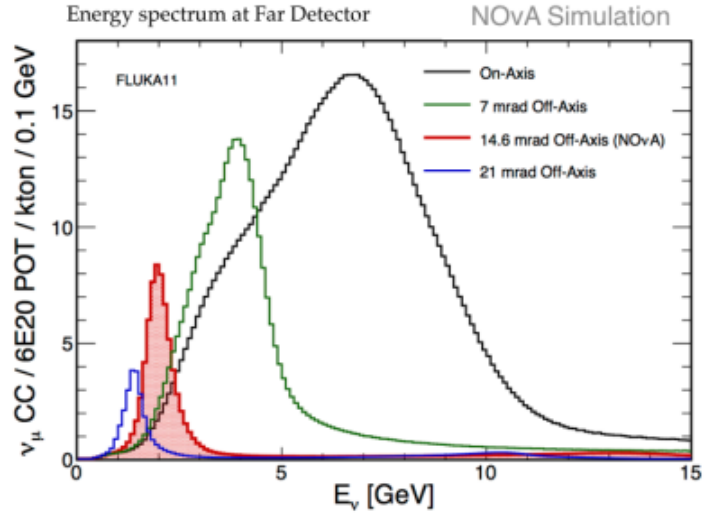
Figure 2.8: Possible neutrino energy spectra as a function of various off-axis angles that would be seen in the Far Detector.

2.6 NOvA Data Quality

The data measured at the Near Detector is used to accurately determine the expected rate at the Far Detector in order to eventually measure the electron-neutrino appearance rate in an almost pure muon-neutrino beam. It is very crucial to have automated and accurate monitoring of the data recorded by the detectors so that the quality of data-taking, which could be affected by issues in the hardware system, DAQ, or beam in the detector channels, can be determined. The Data Quality (DQ) is a series of fully automated scripts designed to handle data processing and data transfer to a permanent disk. DQ is developed to monitor the detector performance and dictates high-quality data selection for physics analyses. It helps determine a collection of events over a time with good data and filters out the channels to be masked prior to the reconstruction. Certain DQ issues severely impact our ability to reconstruct neutrino events and these issues have to be cut out at the analysis level. In this section, the techniques and detector monitoring systems in various stages of data-taking are discussed.

The raw hits collected through the electronics are converted in a human-readable way by Data Acquisition (DAQ) system in the control room which is monitored by the shifter. An event

display (Figure 2.9) shows the real-time state of data-triggered events. Various tools are in place to identify the faulty parts of the detectors. An event display is capable of showing non-reporting DCMs or channels as well as detector timing problems which can lead to broken tracks identified by looking at a few consmic ray tracks that span across the DCMs as shown in Figure 2.10. Each pixel in the event display represents a PVC cell which it lit up when a charged particle crosses the cell and makes a flash of light. The time graph shows the number of hits occuring at a particular time.
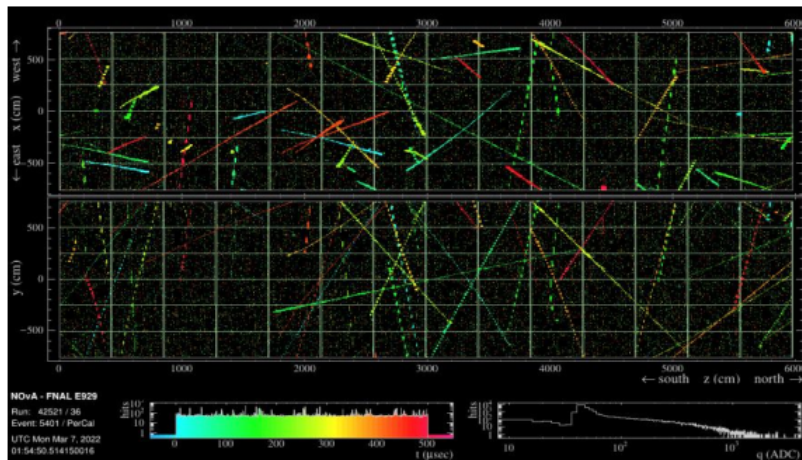
Figure 2.9: A picture of Event Display (FD) with good quality data.
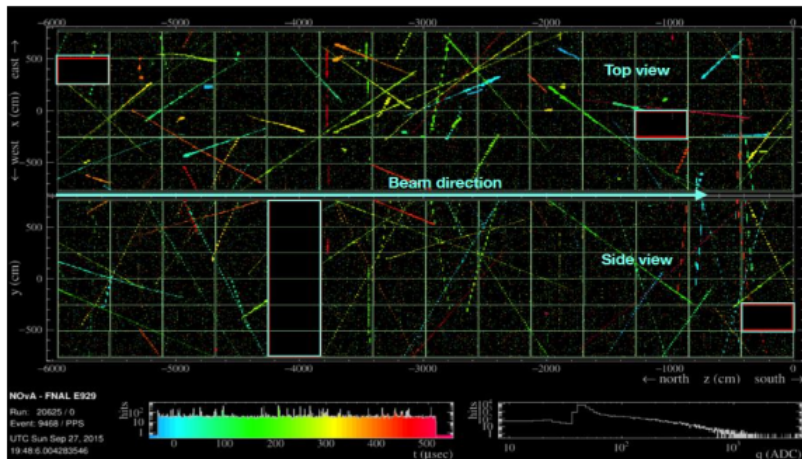
Figure 2.10: The Event Display (FD) would have missing diblocks, DCMs and broken tracks for bad data.

The raw events contains all of the information such as the time and total charge for a particular hit and hardwares like FEBs and pixel number. The nanoslices are associated with individual channels while the microslices are associated with individual DCMs. Each slice is defined as a portion of event zoomed into space and time. The hits are categorized with respect to the charge deposited in terms of Analog-to-Digital Conversion (ADC) in the following way: low for ADC < 175, Minimum Ionizing Particle (MIP) for $175 \leq ADC \leq 3200$ and high for ADC > 3200. A hit rate plot is computed by dividing the hit counts by the total live time. The hit count histograms are filled continuously and the hit rates are recomputed after every 100 processed events. The hit rate plot is another diagnostic tool for DQ. The real time monitoring of live FEBs is shown in green state in the hit rate plot for the Far Detector as shown in Figure 2.11. A bad channel is an APD cell which is "hot" (firing too many times) or "cold" (firing too few times) as shown in Figure 2.12.
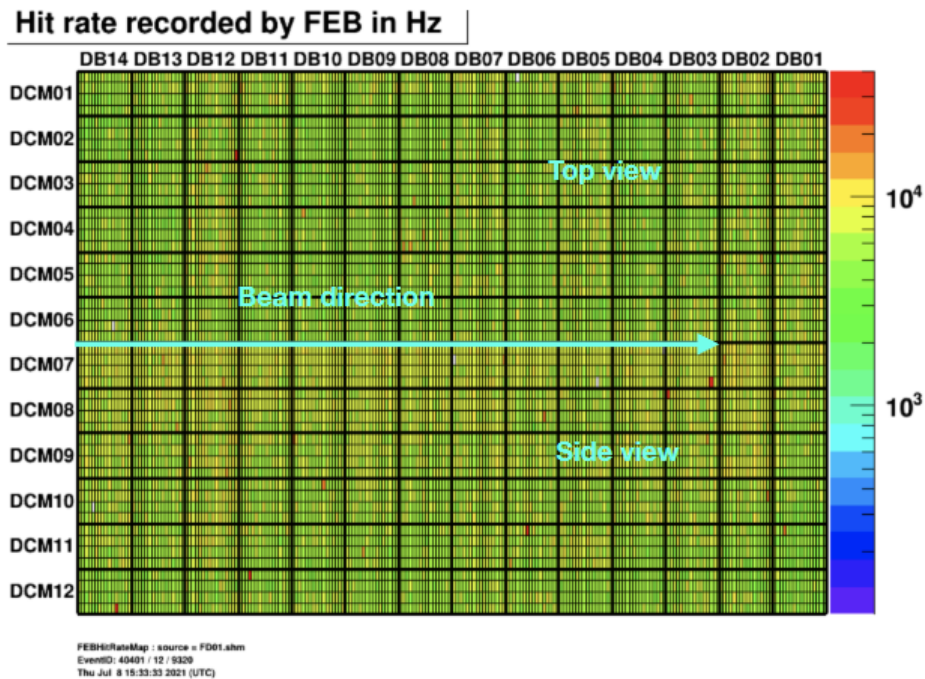
Figure 2.11: As we get the information on hit from data, the hit rate is recorded by FEB in Hz.
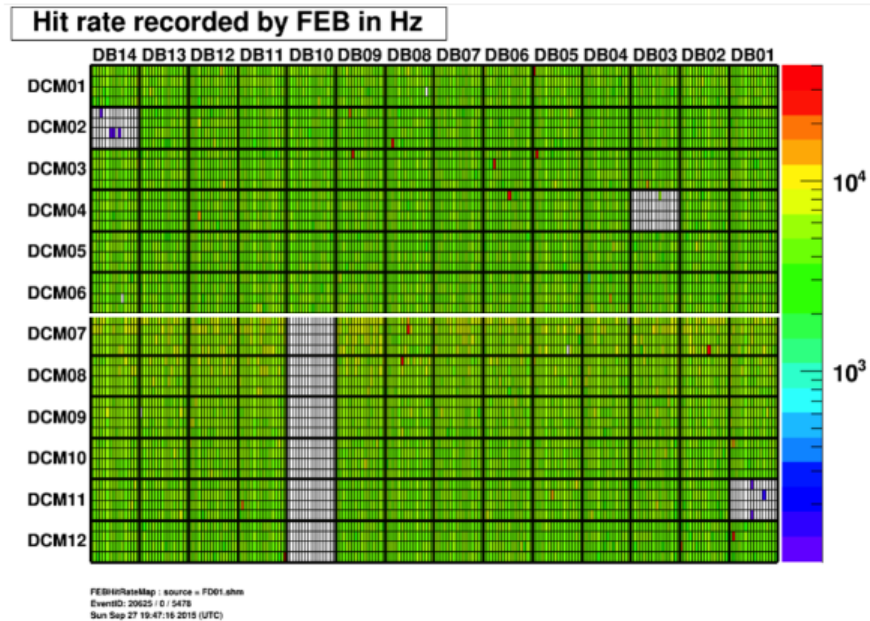
Figure 2.12: Some of the non-reporting DCMs (empty square boxes) suggesting bad data collection.

Another DQ metric to ensure a collection of good data is FEB dropout. The FEB dropout map is monitored to record the number of dropouts and these FEBs have to be replaced. The FEB dropout is basically how many times each FEB switches from a reporting state to a non-reporting state. In simple terms, it is defined as FEB reporting no hit for 1000 events after reporting at least one hit for the previous 1000 events. The FEB dropout is triggered by various factors such as detector crash, power bumps, thunderstorms and even when the cell-phones are not in an airplane mode when it is close to the detector. The cause of FEB dropouts can be identified by looking at the pattern of FEB dropout in the FEB dropout map. The following diagrams in Figure 2.13 show what good data collection and what the patterns for different causes of FEB dropouts look like:
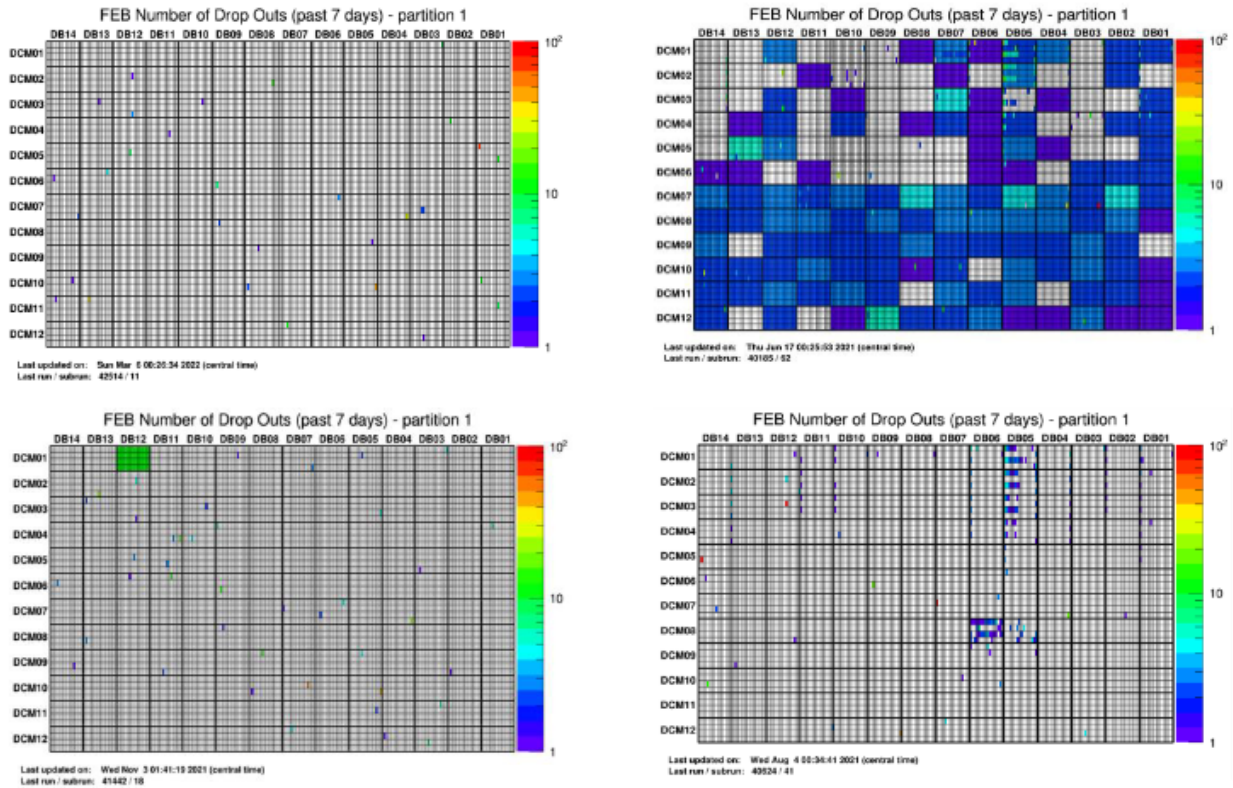
Figure 2.13: Good data collection with extrmely small number of FEBs dropping out (top left), FEBs dropout pattern due to a FD crash (top right), FEBs dropout pattern due to a power bump (bottom left), FEBs dropout pattern due to thunderstorm in Diblock 5 DCMs 1-4 and FEBs dropout pattern due to cell-phone in Diblock 6 DCM 8 (bottom right).

An important DQ metric that shows different data quality failures is the Good Runs plot. Good Runs are basically the scripts that define the criteria for good data-taking. It's an important tool used for the identification of various issues in the detector and provides information on the efficiency of our detectors and data-taking. The Good Runs plot is basically the number of subruns plotted against time. The quality of data is determined to be good if there is no colored column in the plot as shown in Figure 2.14 for the Far Detector. The efficiency of the Far Detector in such situation is at 100% as showin in Figure 2.15.

Various fail modes in the detector are denoted by colored columns in the Good Runs plot as shown in Figure 2.16. The orange column represents Failed Reco that occurs when there are too many or too few tracks in both detectors. This usually happens when one or more DCMs are down in both detectors. The blue column represents Failed Hit and this happens if the median hit rate is

31

too high or too low. In the Near Detecor, it usually takes place when the beam is very unstable. The red column represents Partial Detector fail mode and the green column represents Failed Diblock. These issues happen when a part of the detector in both detectors goes missing or a part of the detector in both detectors has too high or too low hit rate. General causes for these fail modes are detector crash, thunderstorm, diblock issues, etc. The black column represents Failed Other which happens when there is an incorrect timestamp or no activity. One of the general causes is also a change in Daylight Saving Time where the timestamp in the detector either jumps ahead or lags behind by an hour. The purple column represents Failed Live Time that happens when there are less than 1000 triggers in a particular run. In the Near Detector, this fail mode is usually seen when a subrun has low protons-on-target (POT).

The detector monitoring is performed twenty four hours a day through three people each on an eight hour shift. The shifters look at the Data Quality and Good Runs plot to understand the performance and working of the detectors. Any issues arising in the detector are indicated by the Data Quality and Good Runs plots. These issues are then notified to the experts and are promptly addressed.
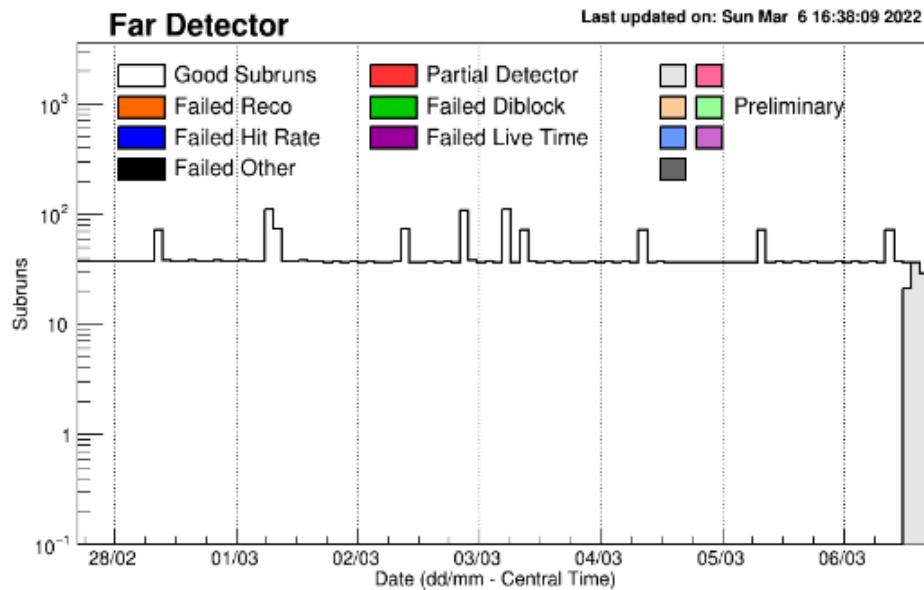
Figure 2.14: The Good Runs plot for Far Detector when there are no detector issues.
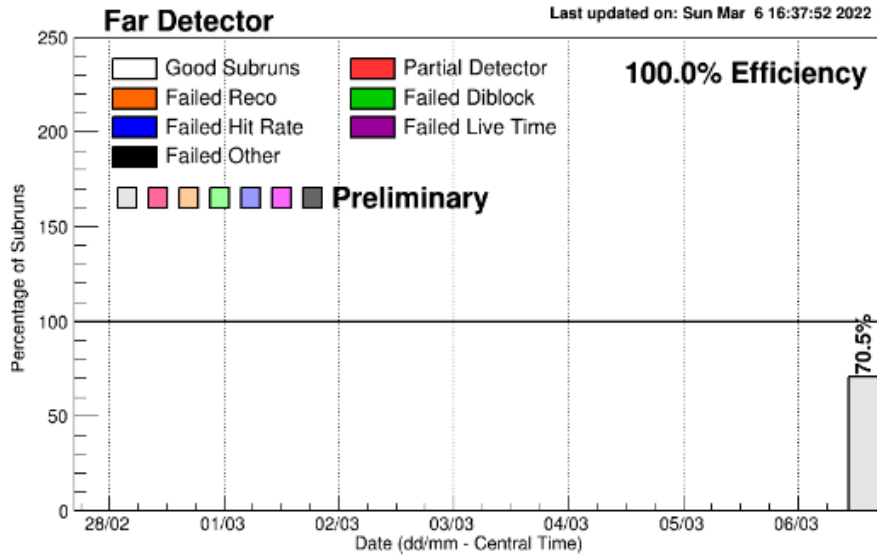
Figure 2.15: The efficiency of Far Detector is at 100% when there are no issues.
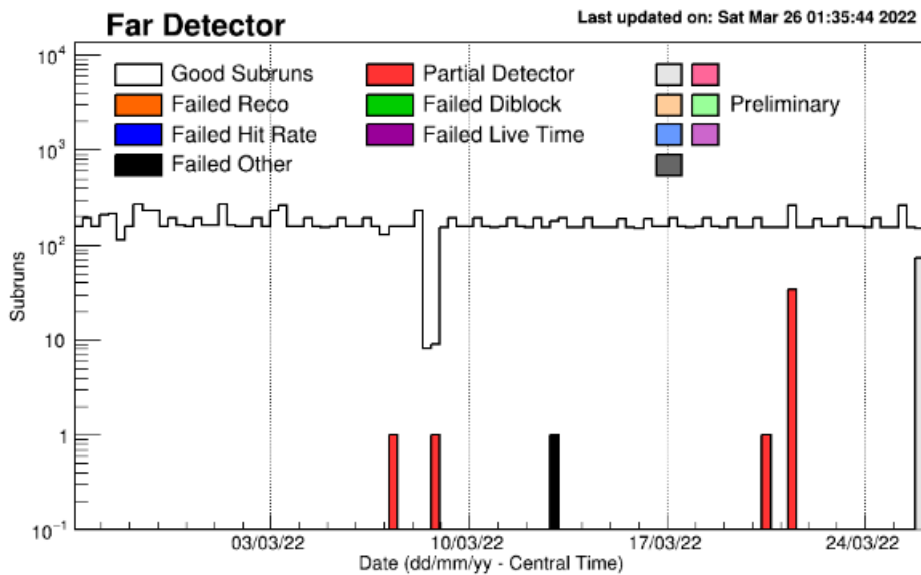
Figure 2.16: Various fail modes are represented by colored columns in the plot. In the given plot for Far Detector over three weeks time, Partial Detector, Failed Reco and Failed Other are the fail modes seen.

2.7 Service Work to NOvA Experiment

As a part of service work to the NOvA experiemnt, I worked as a Good Runs (GR) expert from January 2021 to November 2022. The responsibilites primarily included presenting the weekly Good Runs report at the Data Quality meetings, keeping the Good Runs wiki updated and logging in the ECL any changes pertaining to Good Runs made in the NOvA Data Quality machine in terms of documentation. In terms of database, a part of the responsibilities also included manually marking the bad runs when indicated by Data Quality experts or run coordinator. Another role was to tag the database before publishing new Good Runs Lists (GRL) when indicated by Data Quality conveners, usually before a production campaign. It was also my responsibility as a Good Runs expert to generate, publish and maintains Good Runs Lists. In terms of processes, my responsibility was to develop the Good Runs framework as required by the Data Quality group and update the Near Detector and Far Detector Build Metrics Tree files when switching to a new release.

CHAPTER 3

THE NOvA TEST BEAM

3.1 Introduction to NOvA Test Beam

The NOvA Test Beam is a scaled-down version of the two main NOvA detectors, about 20% the size of the Near Detector, operated to address some of the dominant systematic uncertainties that affect NOvA's analyses. The Test Beam (TB) program was launched in 2019 to improve the understanding of two main NOvA detectors. It was established to get an insight into the detector's hadronic and electromagnetic shower response, light yield, and optical transportation as well as the discrepancies between data and Monte Carlo (MC) simulations in the modeling of the detector. In addition, it will also collect data to build large libraries of the identified particles at well-known energies, which helps in the development of better data-driven PID algorithms for NOvA's analyses.

Far Detector:
896 Planes
14 kton
60 m x 15.6 m x 15.6 m.

Near Detector:
214 Planes
290 ton
16 m x 4.1 m x 4.1 m.

Test Beam Detector:
63 planes
30 ton
4.2 m x 2.6 m x 2.6 m.
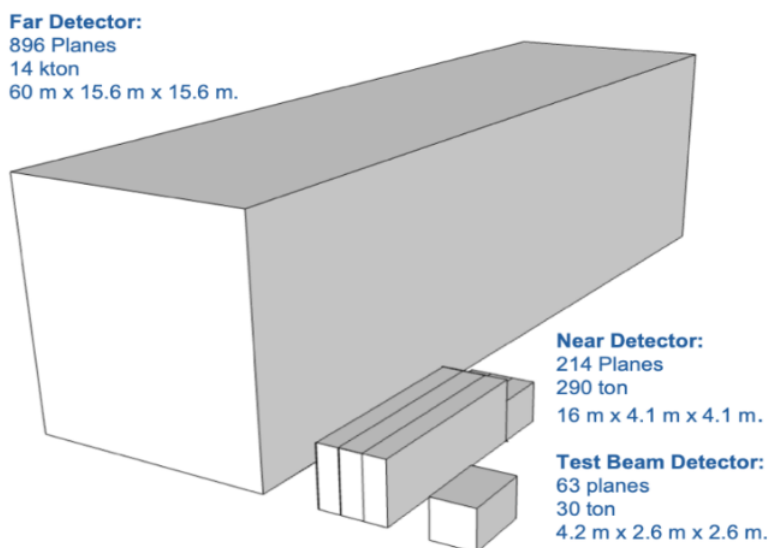
Figure 3.1: Comparing the Test Beam Detector with the two main NOvA Detectors, Far Detector to the left and Near Detector at the centre.

3.1.1 Motivation

The primary objective of the NOvA experiment is to measure neutrino oscillation parameters. Energy measurements of neutrinos at the Near and Far Detector are performed to further measure the disappearance of a muon neutrino (ν_μ) as well as the appearance of electron neutrino (ν_e). Neutrinos interacting through Charged-Current (CC) interaction produce a lepton of the corresponding flavor and hadronic shower. Simulation techniques are employed to identify and differentiate the components. In addition, these simulation techniques are also employed while calibrating the energy which gives rise to uncertainties in the energy resolution. Figure 3.2 shows different types of uncertainties associated with the measurements of neutrino oscillation parameters.
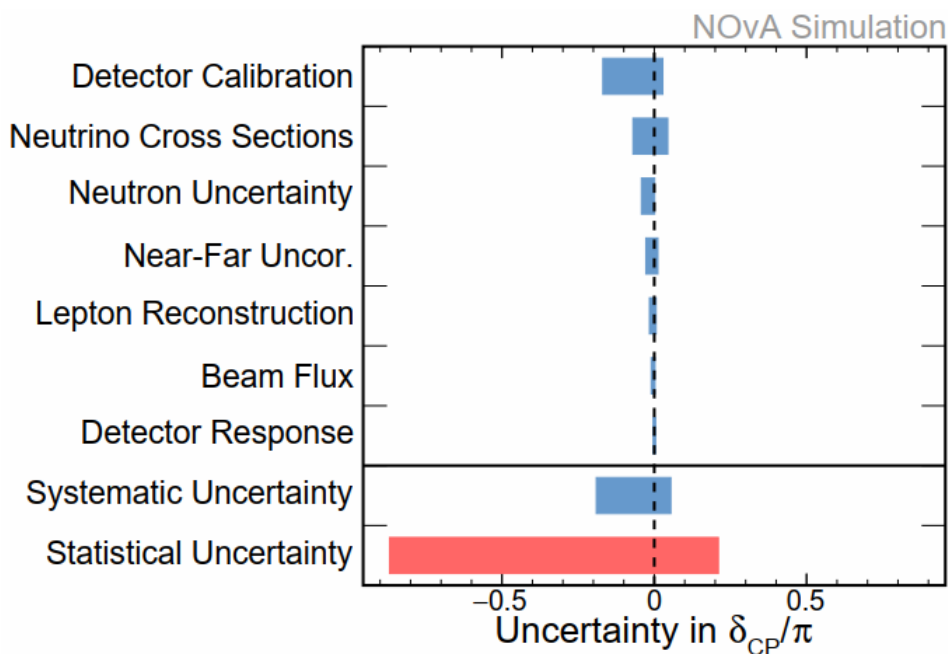
Figure 3.2: Different systematic categories contribute to uncertainties associated with the measurement of δ_{CP}/π.

As shown in Figure 3.2, uncertainties in detector calibration are the leading systematic uncertainty associated with the measurement of neutrino oscillation parameters. Additionally, the oscillation analysis is also affected by lepton reconstruction and detector response systematics, which are also additional uncertainties related to energy. In order to increase accuracy and confidence in the measurement of oscillation parameters, the experiment desires a reduction of these

systematics. The Test Beam program was launched with the goal of reducing these energy-related systematics by understanding the performance of the detector in a better way and improving the simulation techniques employed. The information about a particle is known in Test Beam before it enters the detector, contrary to Near and Far Detector where particle energy is measured in the detectors. This information is very useful in measuring and understanding the response of the two main NOvA detectors to the known particles.

The Test Beam program aims to study the detector response to hadron, muon, and electromagnetic showers in comparison with simulation mode. The studies also include establishing an absolute energy scale, determining energy resolution, and studying topological features, resolution, and particle signatures. Additionally, the Test Beam program also aims to understand light yield and response which involves investigating and understanding Cherenkov light contributions, fiber attenuation, and Birks constant. It also focuses on building a large library of different types of particles at known energies and angles of incidence to employ machine learning techniques in order to identify particles seen in the detector[20].

3.2 Components of the NOvA Test Beam

The NOvA Test Beam is constituted of three main components: (i) Beam from Fermilab Accelerator Division, (ii) Tertiary Beamline components, and (iii) Test Beam Detector. The different components that constitute the NOvA Test Beam are described below:

3.2.1 Beam

The beam to the NOvA Test Beam experiment is delivered by the Accelerator Division (AD) at Fermilab (Figure 3.3 and 3.4). It starts out with a 35 KeV H^- ion source with 100 μs long pulses at a rate of 15 Hz. The beam is focused with the help of an electric field. The ions are then accelerated, with the help of a Radio Frequency Quadrupole (RFQ), to 400 MeV through drift tubes and Radio Frequency stations. The beam then goes into the Booster ring and through a stripping foil to remove the electrons which results in a beam of protons. Protons are then accelerated to 8

GeV. Protons are then sent to the Recycler down the MI-8 line from the Booster. In the Recycler, the bunches of beams are merged together, which are then extracted to the Main Injector, where the protons are accelerated to 120 GeV using the electromagnets.
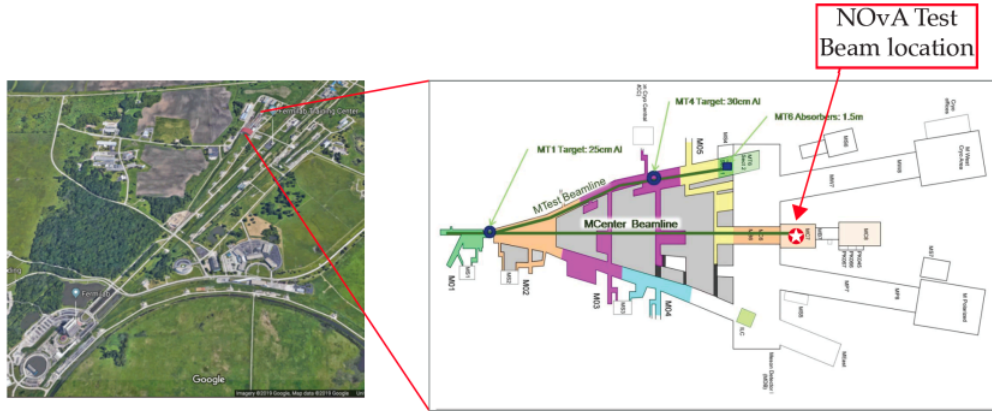
Figure 3.3: A view of Fermilab Accelerator Divison (left) and Fermilab Test Beam facility (right).
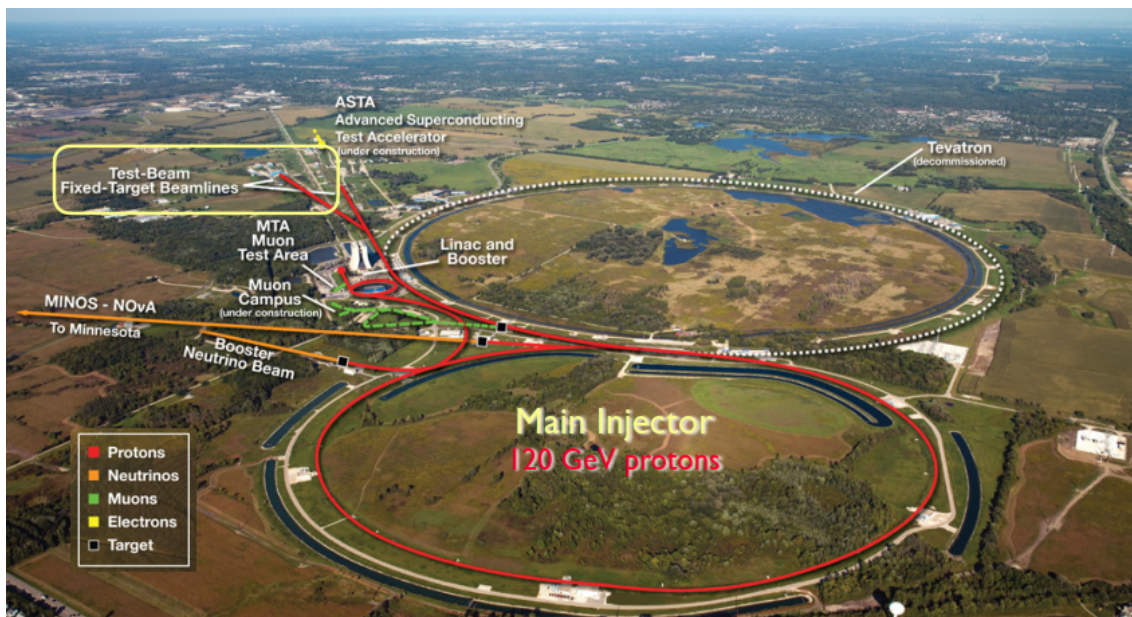
Figure 3.4: Accelerator complex at Fermilab.

Protons with an energy of 120 GeV are sent down to the Neutrino at the Main Injector (NuMI) beamline which is directed to the NOvA Near Detector. For the Test Beam experiments, a resonant extraction resulting in a long, low-intensity pulse sends the beam to Switchyard. With the help of this extraction, we can spread out the 11 μs pulse we receive in the NuMI beamline to the

same amount of intensity in a 4.2 μs pulse. Once the beam reaches the Switchyard, it is split using electrostatic splitting septa. The beam is then sent to the Switchyard beam absorber or MCenter beamlines. NOvA Test Beam is located in the MC7b enclosure. It uses the MCenter beamline and the beam spill consists of 1.6 μs length pulses of the beam, with a total spill length of 4.2 s and spaced 11.2 μs apart. The beam spill containing 1.6 μs length pulses of the beam is referred to as "buckets" and these buckets are not all equally filled since the resonant extraction is not uniform[21].

Once the beam is in the MCenter beamline, the protons are directed to a copper target. The resulting beam is a secondary beamline of 64 GeV, mostly of which are just protons and pions. For the majority of data-taking, the beam with a momentum of 64 GeV/c was used after performing some scans. Various secondary collimator openings were used in order to maximize beam triggers while simultaneously minimizing the shutting off of the detector electronics due to high particle rates.

Upon reaching the MC7b enclosure, the beam is directed to another copper target just 14 m upstream of the Test Beam detector. This is where the tertiary beamline begins. The momentum of the tertiary beam is in the range of 0.2 - 2.0 GeV. The tertiary beam is comprised of characteristic charged particles such as protons, electrons, kaons, pions, and muons. The momentum range of these tertiary beam particles is what we generally observe at the Near and Far Detectors. These well-known particles are selected in the given momentum range with the help of a dipole magnet. The particles then go through a set of other detectors for identification purposes by type and momenta before they enter the NOvA Test Beam Detector, which is placed downstream of the target[21].

3.2.2   Tertiary Beamline

A tertiary beamline mainly contains five main components: time of flight system, analyzer magnet, wire chambers, collimators, and Cherenkov detector as shown in Figure 3.5. The purpose of establishing a tertiary beamline is to identify the type of particle that enters the beamline and measure their properties. The dipole magnet selects the particles in a given momentum range;

wire chambers measure the exact location of particle for reconstructing the particle trajectory and finding their momenta; time of flight system is used to measure the speed and thus the time taken by a particle to reach from one end to the other for particle identification purposes. Collimators are placed to reduce secondary beam spray on the detector and beamline particles. Additionally, there's a threshold Cherenkov detector placed to tag the electrons passing through. Particles can be identified and labeled based on all of this information. All of these components are further described in detail.
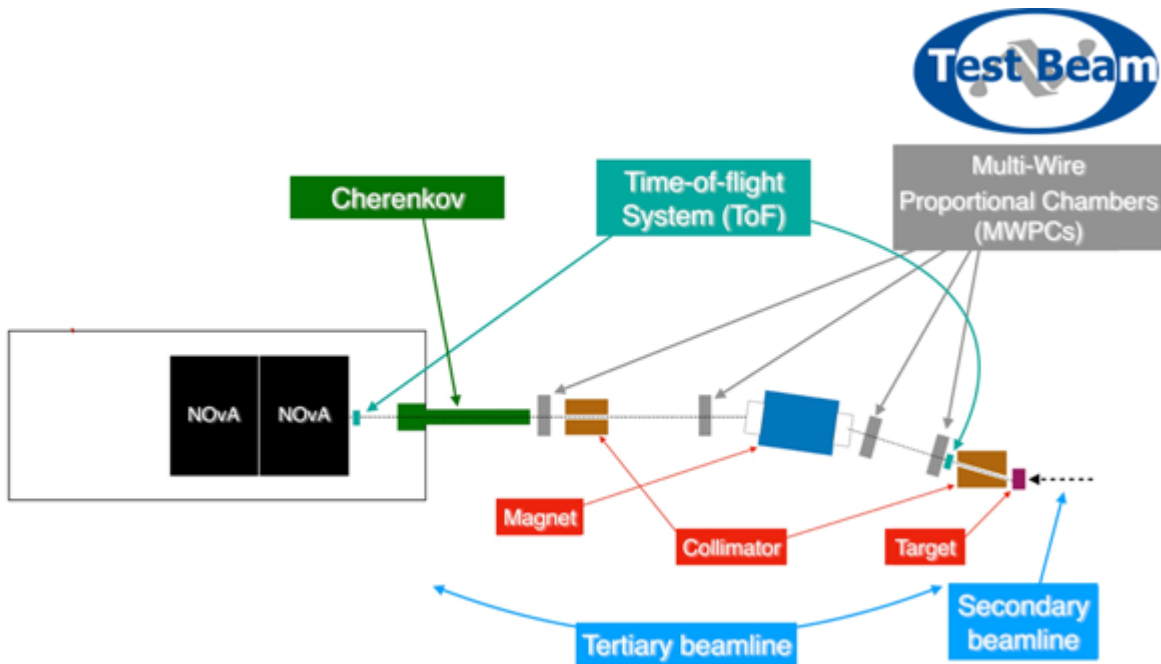
Figure 3.5: Schematic diagram of tertiary beamline components.

3.2.2.1   Time of Flight System

The Time of Flight (ToF) system is established to measure the time taken by a particle to travel between two ToF detectors. Three ToF arms were placed for the same purpose: Upstream (US) ToF using Photo Multiplier Tube (PMT), Downstream-1 (DS-1) ToF using PMT, and Downstream-2 (DS-2) ToF using Silicon Photo Multiplier (SiPM). There were initially two ToF arms before 2021: DS-1 and DS-2 next to each other at the front face of the detector. After 2021, SiPM was placed and ToF DS-1 was moved further upstream to increase the particle acceptance rate.

Each PMT ToF is 5.91×5.91 in^2, with upstream ToF 0.79 in thick and downstream ToF 0.24 in thick. A single ToF can read up to four signals. The reconstructed time is then calibrated. Calibration accounts for different cable lengths and the electronics delays. The time stamp read by DS-1 ToF is considered to be fixed while the other ToF times are adjusted. A large correction in the time stamp values is required in the US ToF as it is closest to the readout electronics. The length between upstream ToF and downstream ToF is 13.16 m. The ToF detectors provide timing resolution in the order of nanoseconds.
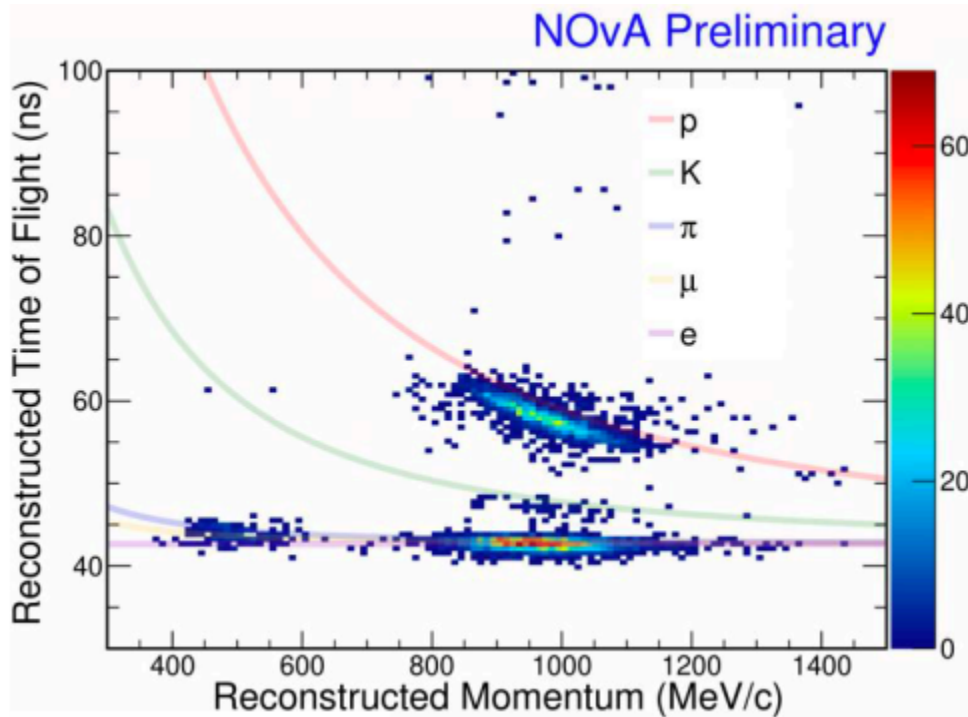
Figure 3.6: A plot showing Reconstructed Time of Flight for different particles plotted against Reconstructed Momentum.

The diagram above in Figure 3.6 shows the measurement of time of flight for different particles at different momentum values. Kaons and protons, the heavier particles, are separated as they require a relatively long period of time to reach from one ToF detector to another. At around 1 GeV/c, it is extremely difficult to distinguish between electrons, pions, and muons as they have similar times of flight.

3.2.2.2 Multi-Wire Proportional Chambers

Multi-Wire Proportional Chambers (MWPCs), or simply wire chambers (WCs), are used to precisely track the position of the particles traversing the beamline. Four wire chambers are placed in the beamline, two being upstream of the dipole magnet and the other two being downstream of the magnet. Each wire chamber is a 5.5" × 5.5" square chamber containing horizontal and vertical planes with 128 gold-plated tungsten wires placed 1 mm apart. The square chambers are filled with a gas mixture of argon, isobutane, and methylal in an 82:15:3 ratio. A constant flow of gas is maintained in the wire chamber. As the particles go through the gas chamber, the gas gets ionized. A high voltage of around 2000 V is applied to accelerate the ionized electrons as shown in Figure 3.7. Isobutane gas neutralizes the Argon ions. As the hits are recorded, a Time-to-Digital Controller (TDC) readout digitizes the time stamp of the hits. As the location of the particle is known from four wire chambers, we can reconstruct the trajectory taken by the particle. Using the known magnetic field, we can also calculate the momentum within $1 - 3\%$ resolution.
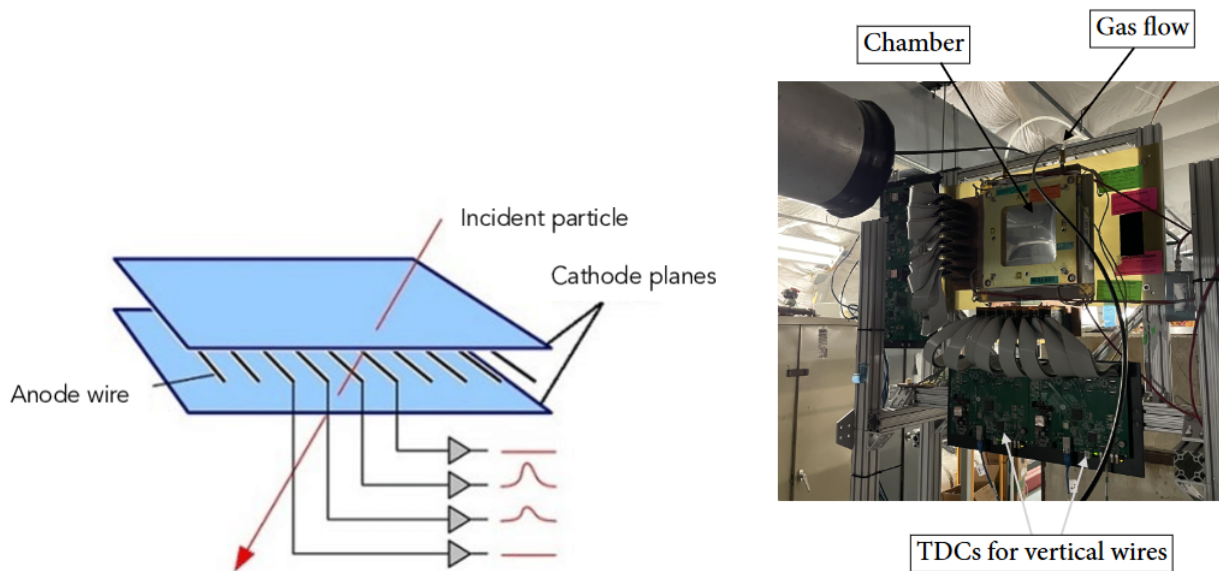
Figure 3.7: Working mechanism (left) and a picture of wire chambers (right).

3.2.2.3 Dipole Magnet

A dipole magnet (Figure 3.8) is an electromagnet used for bending the particles that travel through the beamline. The magnet is placed between Wire Chamber 2 and 3 at an 8° angle with the z-axis along the beamline. The current in the magnet is adjusted to select the particles of the desired momentum. The polarity of the current in the magnet selects the charge of particles. The momentum of a particle can be calculated by using the hit positions in the wire chambers and a parameterization of the magnetic field. For Test Beam analysis purposes, the magnet current of 1000 A, 500 A, and 750 A of both polarities was used.

Figure 3.8: A picture of Dipole Magnet.

3.2.2.4 Cherenkov Detector

The Cherenkov detector is used to differentiate the electrons from other particles in the beamline. It is placed just upstream of DS-2 ToF. The detector is filled with about 250 liters of CO_2 gas at 1 atmospheric pressure. It is L-shaped and made of two stainless steel pipes. Each end of the pipe has two windows: a 0.006 in vinyl window followed by a 0.00175 in tedlar window. A Mylar mirror is placed at 45° angle towards the end of the horizontal pipe. A PMT is placed in the vertical pipe where the mirror can reflect the Cherenkov light. Particles emit Cherenkov light if the velocity of the particle is greater than the speed of light in CO_2.
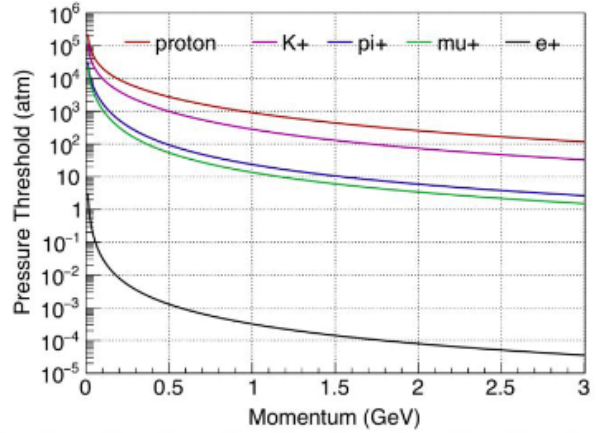
Figure 3.9: A picture of Cherenkov detector (left) [4] and Cherenkov threshold for different particles against the gas pressure inside the Cherenkov detector (right).

The diagram above to the right in Figure 3.9 shows the pressure threshold for different particles to produce Cherenkov light in the given momentum range. For the momentum range of the particles traversing the beamline in NOvA Test Beam, it is seen that Cherenkov light is only emitted by the electrons under 1 atmospheric pressure. At this pressure threshold, the electrons with momentum down to 20 MeV/c can emit a Cherenkov light. Apart from the electrons, the other particles require much higher energies or much higher pressure to produce the Cherenkov light. The Cherenkov light is directed toward the PMT where the signal is amplified and read before passing it on to the digitzer.

3.2.2.5 Scintillator Paddles and Helium Pipes

Four scintillator paddles were placed in the beamline upstream of each multi-wire proportional chamber. These paddles were used for trigger purposes. Triggering on a coincidence of these paddles was much more efficient than triggering on a coincidence of wire chambers.

Helium pipes were placed in the beamline to minimize interactions and energy loss as the particles traversed the beamline. Four helium pipes were initially placed for the same purpose: between wire chambers 1 and 2, between dipole magnet and wire chamber 3, between wire chambers 3 and 4, and between wire chamber 4 and the Cherenkov detector.

3.2.3 NOvA Test Beam Detector

The NOvA Test Beam detector (Figure 3.10) is a scaled-down but functionally identical version of the NOvA Near and Far detectors. The detector weighs 30 tons and the dimensions read 4.2 m × 2.6 m × 2.6 m. The Test Beam detector consists of 31 horizontal planes and 32 vertical planes starting and ending with the vertical planes. The Test Beam detector contains both versions of FEBs from the Near detector and Far detector to study the differences in their response when subjected to the same environment. Out of a total of 126 FEBs, 118 are v4 FEBs which are present in the Far detector and the remaining 8 are the faster version of v5 FEBs which are present in the Near detector to collect data at a much faster rate than the Far detector as it is closer to the beam sources and receives the beam with higher intensity. A single FEB reads out 64 cells.

Figure 3.10: A picture of NOvA Test Beam detector placed in MC7b enclosure at the Fermilab Test Beam Facility.

Horizontal and vertical cells are arranged alternatively in the Test Beam detector and these cells are filled with a scintillator. The first half of the detector is filled with a scintillator left over

from NOvA proto-type detector; the majority of the second half of the detector is filled with a scintillator left over from the Far detector and a few planes towards the end contain scintillator supplied by the University of Texas at Austin.

3.2.3.1 Test Beam Setup, Commissioning, Data Acquisition (DAQ) and Data-taking Summary

The Test Beam program collected data between March 2019 and July 2022. The detector was started to be filled with a scintillator in April 2019. It was permitted to receive beam and operate 24/7 in the final week of May later that year. The Test Beam detector received the first beam in the first week of June 2019. During the commissioning period, only 15 days of the beam were recorded. This period was followed by a beam shutdown in the summer of 2019. During the beam shutdown period, the rest of the detector was outfitted with electronics. The first cosmic data with the active full detector was taken in November 2019. In December 2019, the beam returned to the Test Beam detector, the beginning of Period 2 data-taking. The trigger was switched to a ToF-based trigger. In order to increase the efficiency of the triggers, it was decided the trigger would be on the coincidence of scintillator paddles placed upstream of each wire chamber. It was followed by beam-related changes, FEB firmware changes, secondary beam intensity scans, secondary beam momentum scans, and collimator scans. A long beam shutdown followed thereafter in March 2020. Concrete blocks were installed upstream of the tertiary beamline to shield some of the high-energy muons to account for the electronics shutoffs. In January 2021, the beam returned back to the Test Beam for Period 3 data-taking. In Period 3, beam tuning was performed which eventually resulted in a good particle rate at the beginning of March. There was a further increase in particle rate as a result of more tuning towards the end of March. ToF cuts for particle selection were also adjusted as the downstream ToF was moved from its original location to be placed just before the Cherenkov detector. Different ToF cuts were implemented based on the particles' momentum at 500 MeV/c, 750 MeV/c, and 1 GeV/c. The dipole magnet current polarity was mostly positive for Period 3 data-taking which selected positively charged particles. The final data-taking period, Period 4, began in November 2021 and lasted up to July 2022 with the Test Beam detector being

decommissioned afterwards. The analysis in the following chapter contains data from Period 3.

During the commissioning period, modules were developed to unify beamline and detector simulation. GEANT4[22] was primarily used for beamline simulation while particle information collected from data was used as a text input file to make detector simulation files. The module was developed in a way to read from beamline simulation and add the information to the detector simulation. The development of Data Acquisition (DAQ)[23] code began in the spring of 2018. FEBs were put to test the working of DAQ even before the detector was fully assembled. The Test Beam data acquisition involves two separate systems: NOvA Detector DAQ for collecting the data from the NOvA detector and NOvA Beamline DAQ for collecting the data from the beamline detectors. Each DAQ system consists of a Timing Distribution Unit (TDU) to timestamp the collected data. There are spill server triggers to trigger the data collection in the detector. Similarly, beamline TDU timestamps the beamline data marked by a 64 MHz clock. An 8-bit signal from the Fermilab Accelerator Division is taken as an input for beam timing using the GPS system. The beamline triggers are managed by a CAEN V1945 trigger board which takes input from the Cherenkov detector, ToF, wire chambers, and scintillator paddles and provides trigger outputs to the digitizer, TDUs, and wire chamber controllers to initiate data readout and digitization. The most efficient triggers are on scintillator paddles, four of which are placed before each wire chamber. Triggers occur when a particle passes through these four scintillator paddles. In the Test Beam detector, data is saved for three different triggers: i) Beamline trigger, ii) Activity trigger, and iii) Spill trigger. The data collected with beamline triggers from both beamline and detectors are merged while converting them to NOvASoft data. The data collected with activity and spill triggers are saved into offline formatted data. The data is then reconstructed and calibrated before being used for analysis purposes.

CHAPTER 4

ANALYIS OF ELECTRONS IN THE NOvA TEST BEAM

In this chapter, the analysis of electronic properties from Test Beam is discussed. The purpose of the study is to understand how the detector responds to the electrons and how the electrons behave in the detector using Test Beam data and compare the results to simulation.

4.1   Motivation and Objectives of Electron Analysis

The NOvA experiment searches for $\nu_\mu \rightarrow \nu_e$ flavor oscillation. Since the initial sample of neutrinos is predominantly muon neutrinos, the measurement that actually gives us oscillation parameters is basically associated with the number of electron neutrinos measured at the Far Detector versus how many muon neutrinos. Since the Charged Current (CC) ν_e interactions produce electrons in the final state as shown in Figure 4.1, the critical measurement depends on identifying and measuring these electrons in the Far Detector.
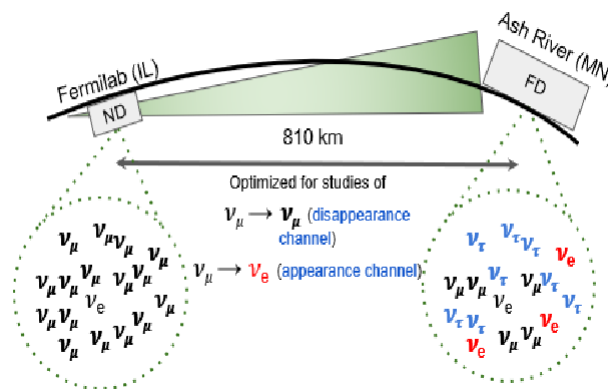
Figure 4.1: The Charged Current (CC) ν_e interactions produce electrons in the final state and the critical measurement of oscillation parameters depends on identifying and measuring the electrons in the Far Detector.

The main goal of studying the electrons in the Test Beam program is to characterize the electron energy response of NOvA hardware. The study helps reduce the uncertainties associated with electrons and also potentially improves the measurements of the electron neutrino ν_e oscillation parameters. The analysis is also important to understand the behavior of the electrons in the two main neutrino detectors.

4.2   Analysis Procedure: Comparison of Data with Simulation

The analysis procedure is summarized in this section. The analysis was performed comparing Test Beam data and simulation as there was a lack of statistics from the Near Detector.

4.2.1   Test Beam Data Selection

The data contains all the electrons collected between January 12 - April 12, 2021, known as Period 3 [24]. Various cuts are implemented to select the electrons from data which are explained as follows:

4.2.1.1   Beamline Cuts for Data Selection

- Events with deadtime are rejected.

- Valid wire chamber track with reconstructed momentum > 0.

- Magnet current of 500 A, 750 A and 1000 A to select electrons with energy 0.5 GeV, 0.75 GeV and 1 GeV respectively.

- For Period 3, the time of flight is 30 ns < Time of Flight < 36 ns.

- Vertical distance of the particle from the center of magnet in the beamline -6.5 cm < Distance from the center of magnet < 9.5 cm.

4.2.1.2   Detector Cuts for Data Selection

- Vertex Position Cut: -20 cm < Track Start Position in X Direction < 20 cm, -25 cm < Track Start Position in Y Direction < 14 cm, Track Start Position in Z Direction < 20 cm.

49

- Hit Time of 50000 ns < Slice Time < 55000 ns.

- Track Length cut of < 150 cm to reject muons traversing straight through the detector.

- Number of hits in detector ≥ 5.

- Track direction cut $\cos(z) > 0.95$ to select only forward going electrons.

4.2.2 Test Beam Simulation

In this subsection, the two procedures to generate Test Beam simulation are discussed. This analysis uses two simulation procedures: i) NOvA Detector Input from Single Particle Generation and ii) NOvA Detector Input from Beamline Generation and Simulation.

The first method uses the simulation files generated by feeding single-particle information as input to GEANT4. The following particle properties are used as an input to generate a particular particle of particular momentum at a given location: pdg code, space components of momentum, energy, mass, start positions and timestamp. A simple script was used to smear the number of electrons to generate enough electrons for meaningful analysis. The real data was mimicked using out-of-time beam backgrounds from actual data by overlaying them on the simulated particle. The particles from simulation are placed at time t = 84000 ns. This time is 30000 ns after a beam spill of particles into the detector to guarentee the particle causing the trigger in data is not contained. Deadtime algorithms are then run on the backgrounds at 84000 ns to make sure the tracks with missing hits are not overlaid onto the data. Finally, the reconstruction algorithm is run over simulation in the same way as for data. This procedure minimizes any bias in the reconstruction algorithm to treat data and simulation differently.
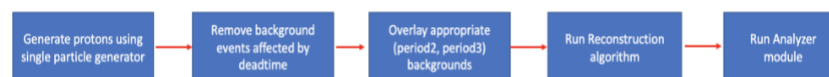
Figure 4.2: A flowchart showing the entire process of Test Beam simulation using Single Particle Generation process.

The second method involves generating particles upstream of and simulating interactions with the beamline components. This is done in two stages: The first stage involves generating particles and simulating the beamline while the second stage involves providing the input and simulating the subsequent interactions within the detector. The beamline simulation is performed by G4beamline, an external software package build on top of GEANT4. An input geometry file is required to define the experimental setup in order to run G4beamline. In this analysis, the updated version of beamline geometry[23] is used.

### 4.2.2.1 Cuts Implemented for Test Beam Simulation

- 82000 ns < Slice Time < 88000 ns. The simulated particle is placed at 84000 ns.

- Vertex Position Cut: -20 cm < Track Start Position in X Direction < 20 cm, -25 cm < Track Start Position in Y Direction < 14 cm, Track Start Position in Z Direction < 20 cm.

- Track length of < 150 cm to reject accidental muons.

- Number of hits in detector ≥ 5 hits.

- Track direction cut $\cos(z) > 0.95$ to select only forward going electrons.

4.2.3 Analysis of the Electronic Properties

The electronic properties are discussed in this subsection. Preliminary results in the form of various plots of electronic properties are presented by comparing data simultaneously with both simulation techniques as discussed above. Prongs have been used in the analysis of the electrons while calorimetric energy, total energy, number of hits, calorimetric energy per hit and total energy per hit in the slice have also been investigated.

4.2.3.1 Slice and Prongs

One of the powerful features of NOvA detector is that it is very easy to cluster activity associated with a common particle in both space and time. This is the first stage of reconstruction known as slicing and is shown in Figure 4.3.
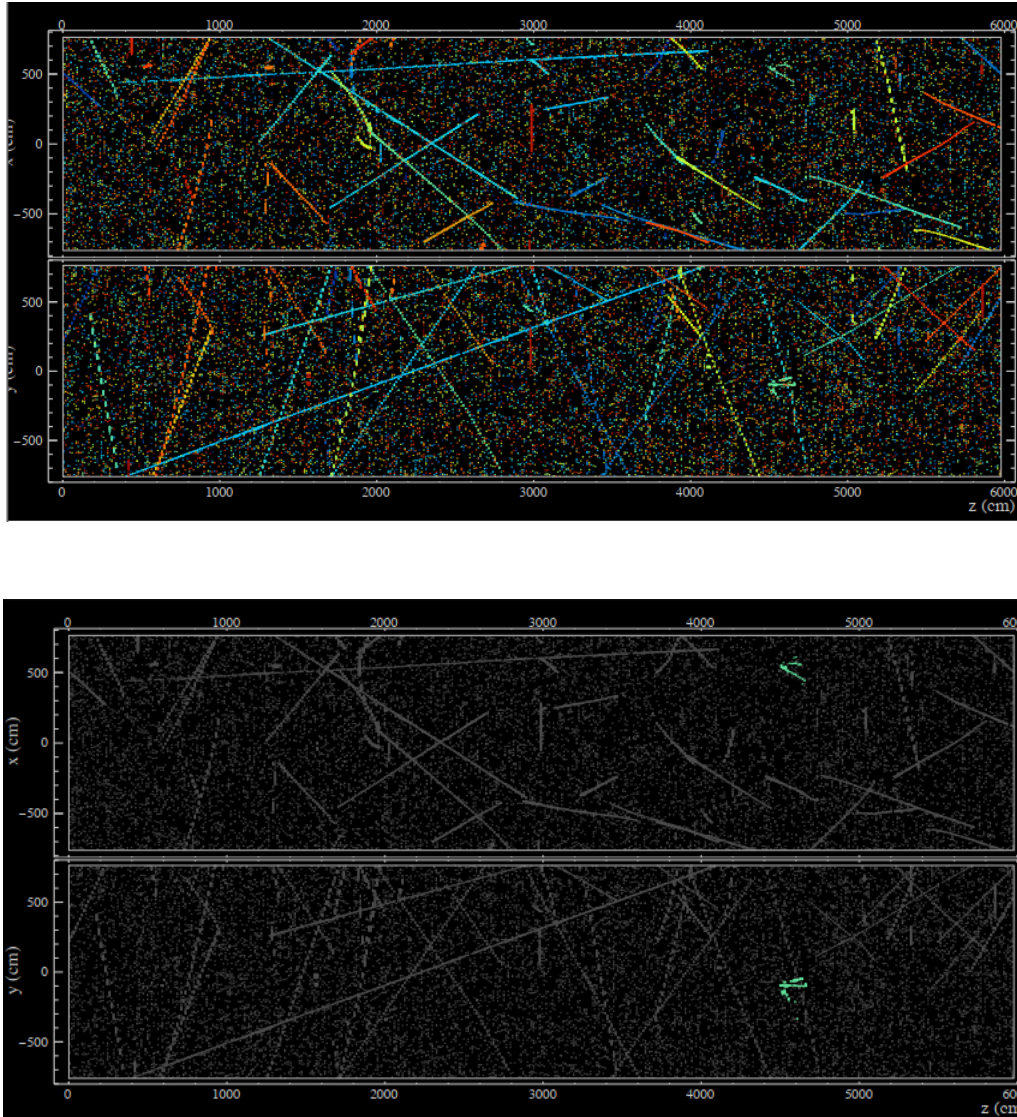
Figure 4.3: An example of slicing from the FD neutrino event. In the second event display, activities associated with antinuetrino NC candidate are clustered in time.

Following slicing, the next step is vertex finding. Vertex finding is done more for neutrino events. It is subsequently followed by a prong finding which groups hits from a particle into a single object known as a prong. Prongs are used in the analysis of electron-like particles that shower and have non-uniform hits distribution in the detector. Matching the hits in between the views leads to 3D objects generally known as tracks[25] as shown in Figure 4.4.
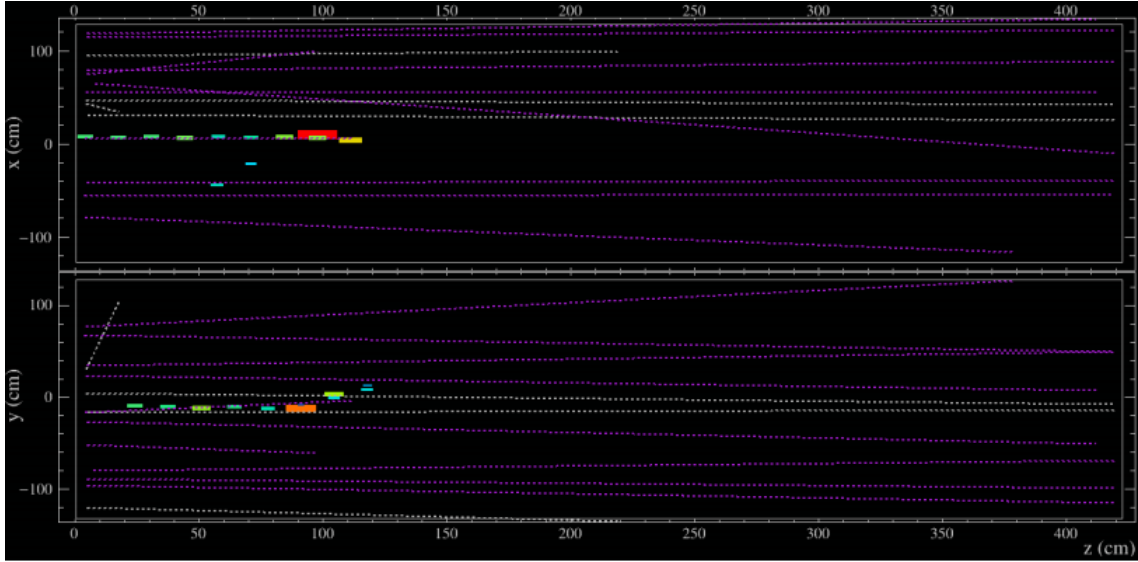
Figure 4.4: Reconstructed objects for the associated event.

4.2.3.2   Analysis

In this subsection, various kinematics plots of the electrons selected from data and simu-

lation are presented and the comparisons are made between data and both simulation techniques.

All the plots shown here have simulation normalized to data.

- **Calorimetric Energy**: It is the energy deposited by a particle in the detector. The plots of

  deposited calorimetric energy by electrons is shown in Figure 4.5 for different magnet current

  configurations. The plots show that while the results from both simulation techniques agree

  to a great extent, there is an obvious disagreement with the results obtained from data. The

  peaks for three different plots are different as expected according to the magnet current

  configurations.
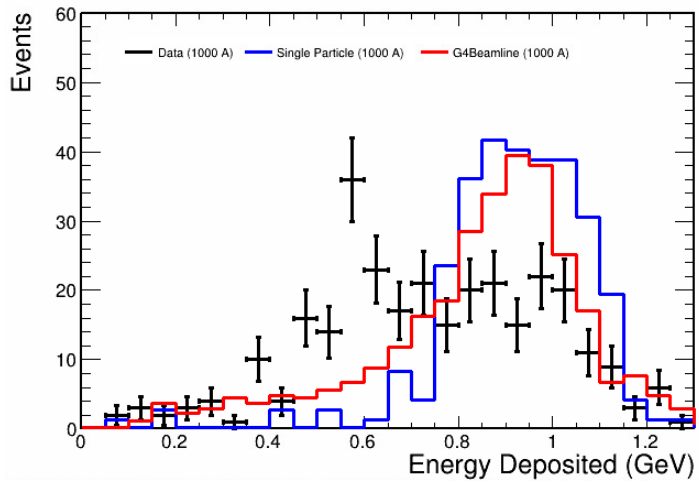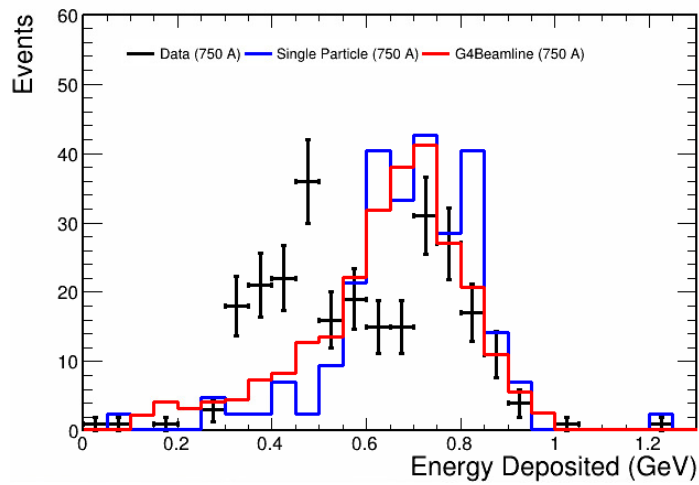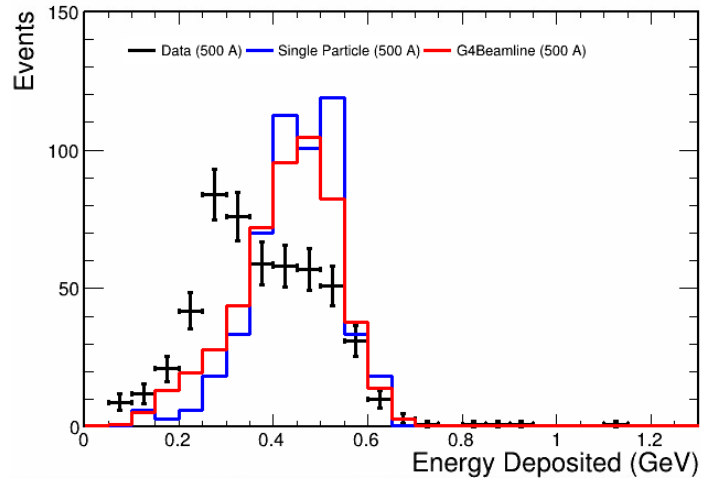
Figure 4.5: Calorimetric energy deposited obtained from data and simulation for different current configurations.

- **Calorimetric Energy in the Slice**: Figure 4.6 shows the calorimetric energy deposited in the slice for three different current configurations. The peak values are again different as expected because of different magnet current configurations. Once again the data is in disagreement with the results obtained from both simulation techniques.
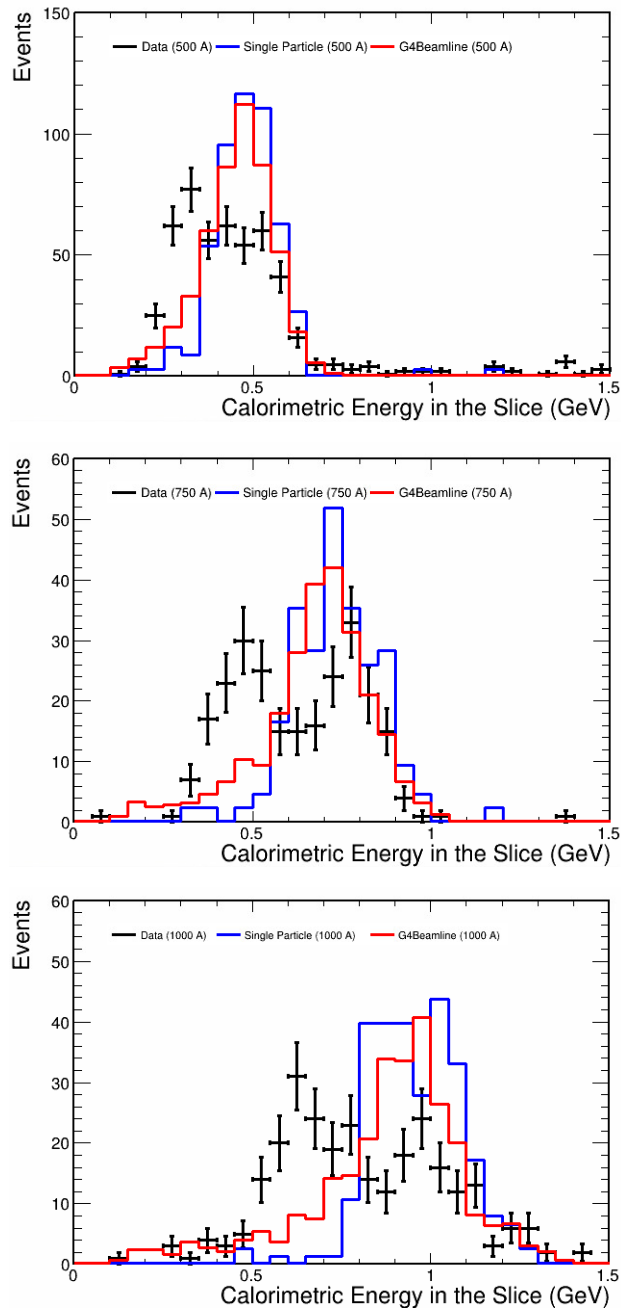

Figure 4.6: Calorimetric energy deposited in the slice obtained from data and simulation for different current configurations.

- **Total Energy in the Slice**: As charged particles in the NOvA detector deposit energy in the liquid scintillator and the rest of detector material is essentially made up of plastic (dead material), we introduce a correction factor of 1.78 to divide the calorimetric energy and obtain the total energy. Figure 4.7 shows the total energy deposited in the slice for three different current configurations. The data peaks in the plots still disagree with the simulation results. The plots read different peak values for different current configurations.
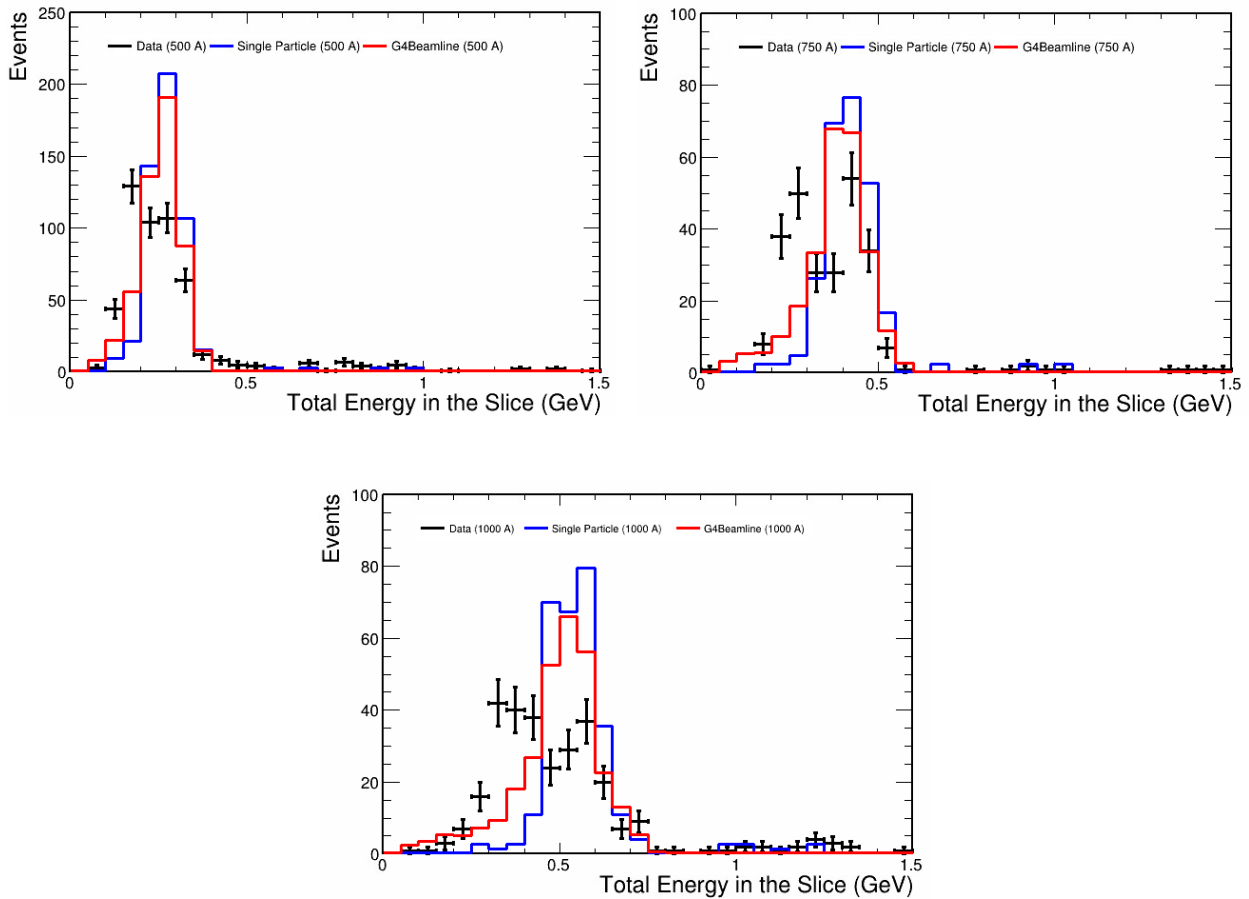

Figure 4.7: Total energy deposited in the slice obtained from data and simulation for different current configurations.

The discrepancy in all the energy variables presented above is quite obvious. In order to account for that, it was necessary to inititally investigate what data and simulation events looked like. Presented below are some of the event displays obtained from data and simulation.
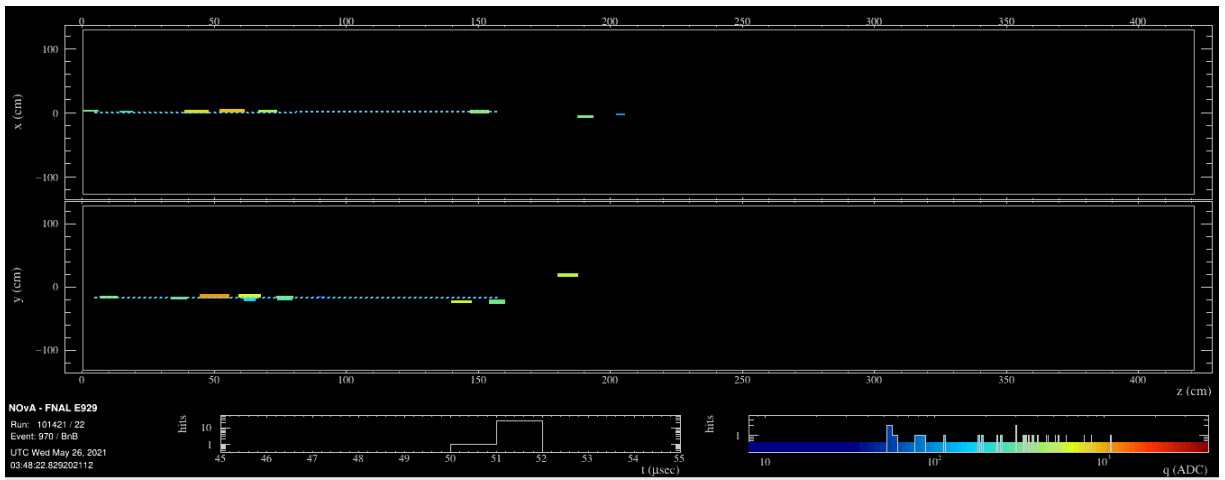
Figure 4.8: An event display with electron candidate event obtained from Test Beam data at 500 A current configuration.
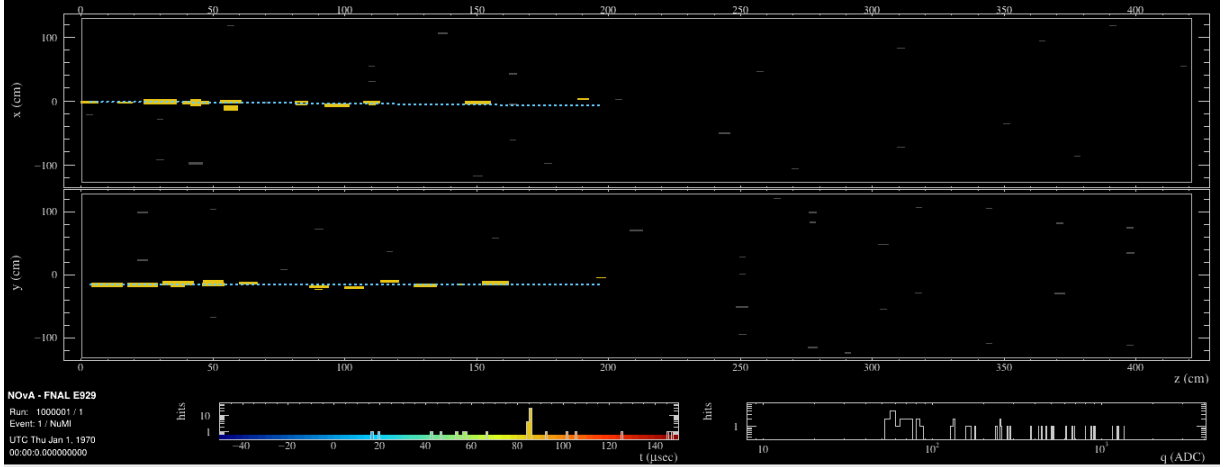
Figure 4.9: An event display with electron candidate event obtained from Test Beam simulation at 500 A current configuration.
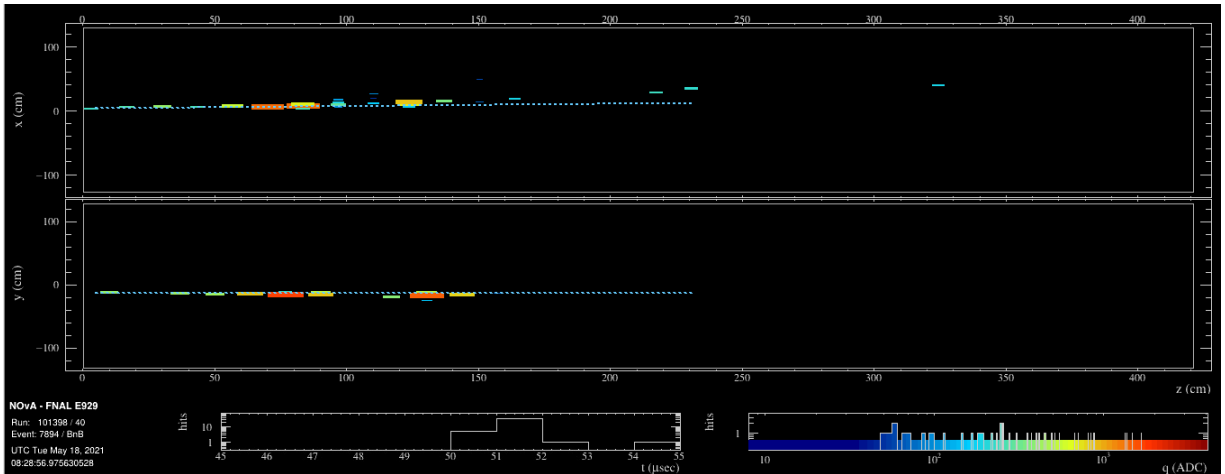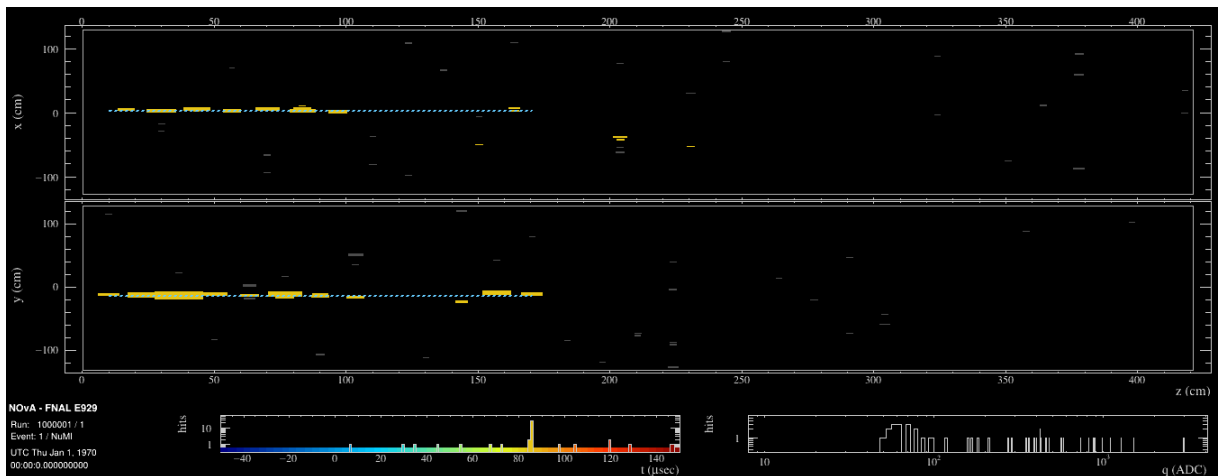
Figure 4.10: An event display with electron candidate event obtained from Test Beam data at 750 A current configuration.
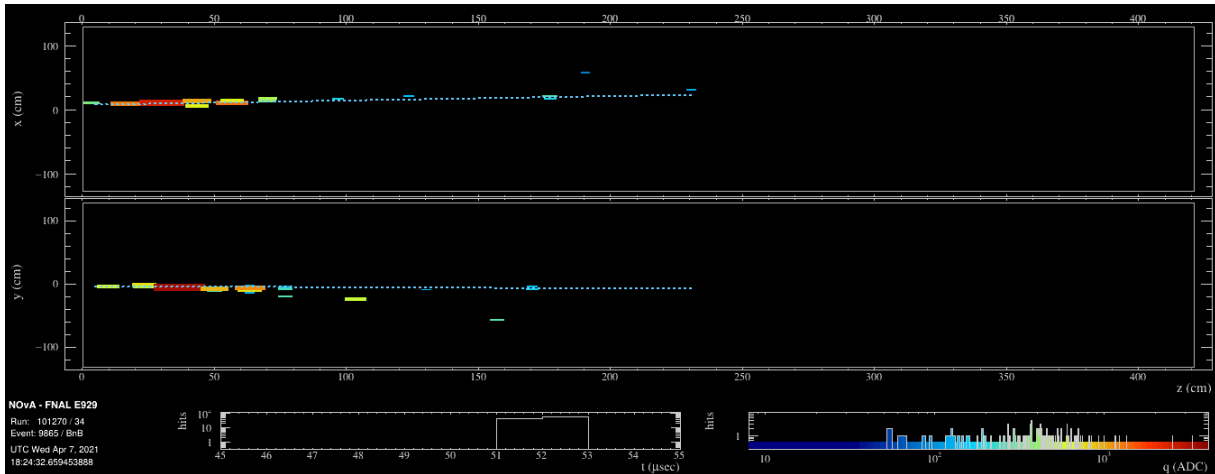

Figure 4.11: An event display with electron candidate event obtained from Test Beam simulation at 750 A current configuration.

Figure 4.12: An event display with electron candidate event obtained from Test Beam data at 1000 A current configuration.

Figure 4.13: An event display with electron candidate event obtained from Test Beam simulation at 1000 A current configuration.
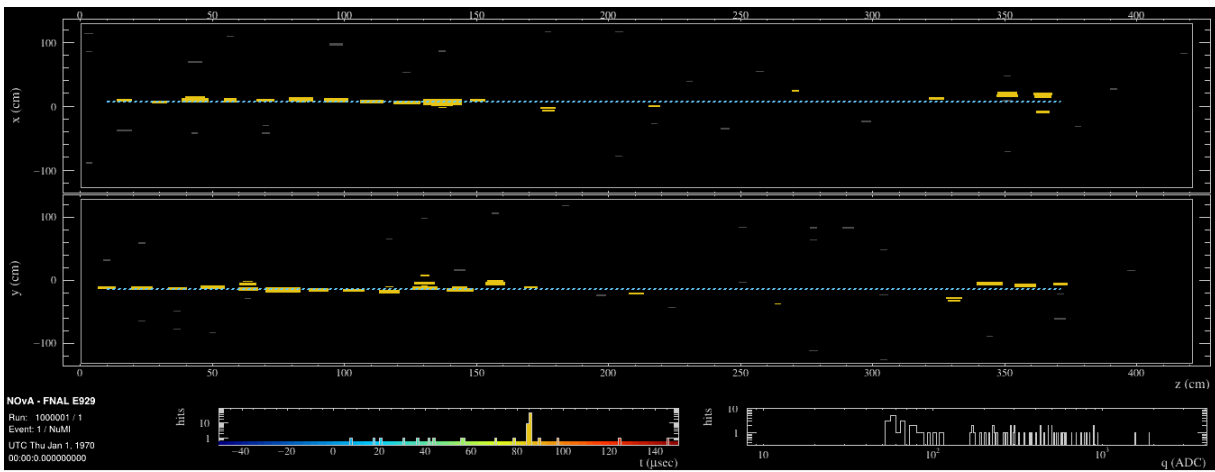
The event displays obtained from both data and simulation for different magnet current configurations show no significant differences between them. It is therefore not possible to single out a cause for the disagreement between data and simulation results for the aforementioned energy variables. It could well be that the calibration is not accurate. Further studies regarding calibration is necessary to address the apparent discrepancy between data and simulation and this is something that is being investigated by the Test Beam group in NOvA.

- **Number of Hits**: Figure 4.14 shows the number of hits obtained from data and simulation for different current configurations. The number of hits show a good agreement between the obtained results from data and simulation except that the peak for data is different than of simulation for 1000 A. The number of hits increase as the current increases as the electrons gain more momentum.
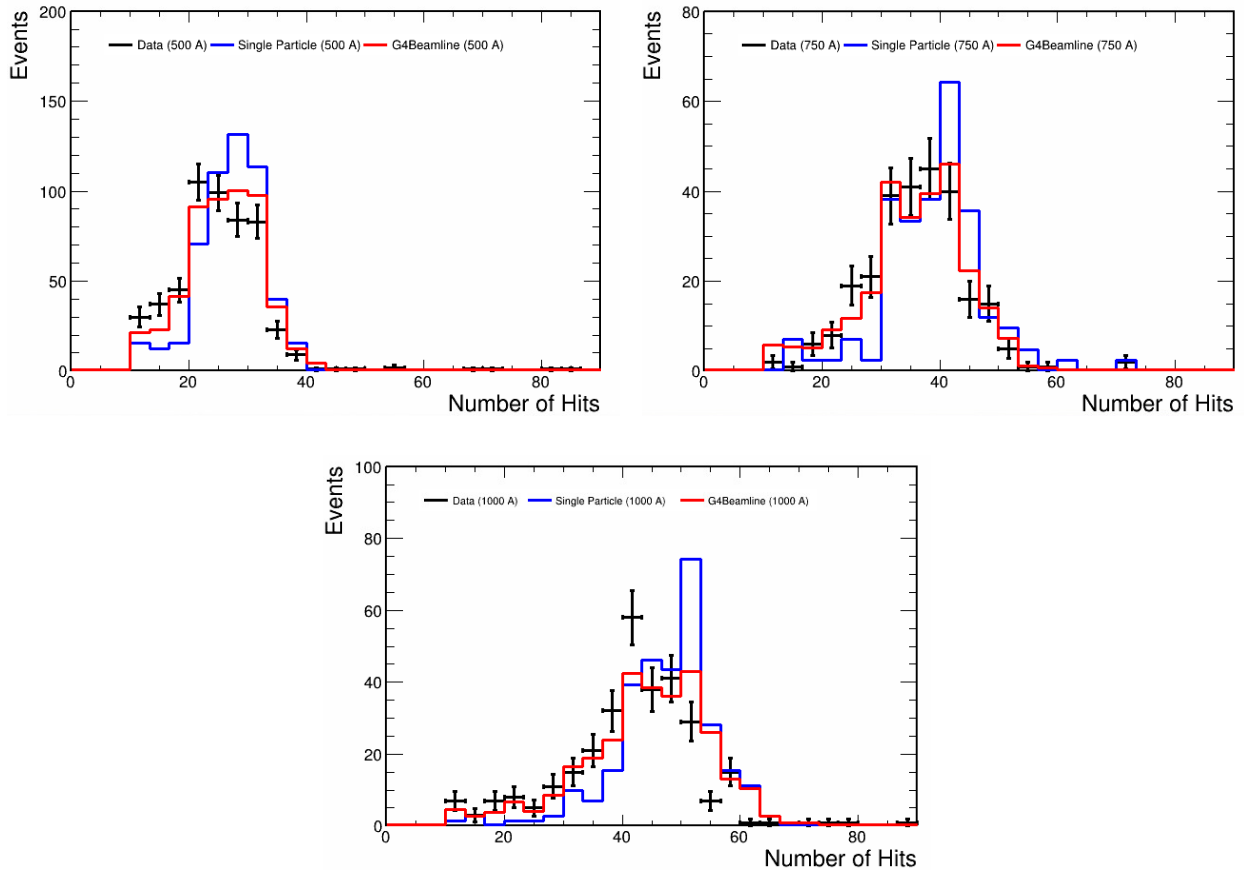
Figure 4.14: Number of hits obtained from data and simulation for different current configurations.

- **Number of Hits in the Slice**: Figure 4.15 shows the number of hits in the slice obtained from data and simulation for different current configurations. The number of hits in the slice show a good agreement between the obtained results from data and simulation except for the peak values in data and simulation for 1000 A. The number of hits in the slice increases as well when the current increases as the electrons gain momentum.
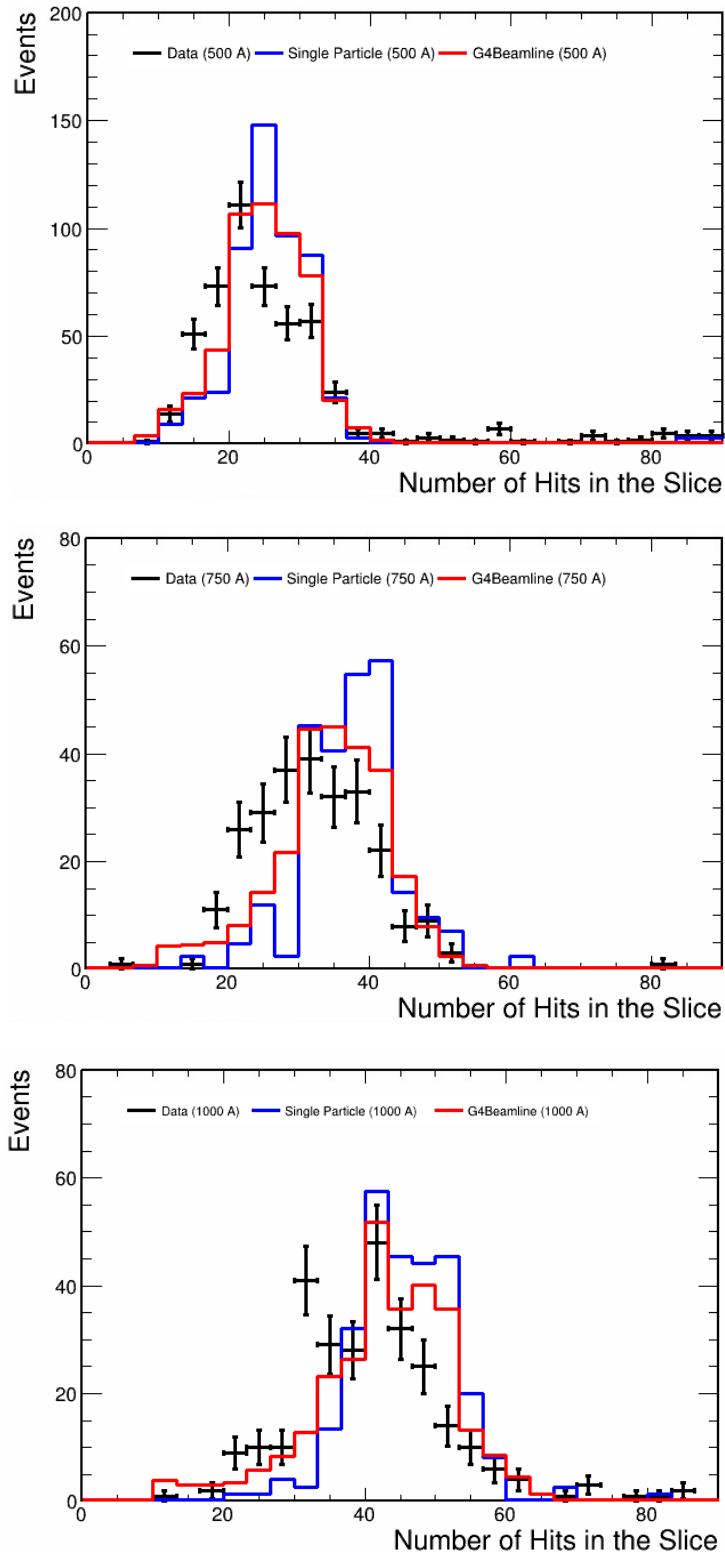
Figure 4.15: Number of hits in the slice obtained from data and simulation for different current configurations.

- **Calorimetric Energy Per Hit**: Figure 4.16 shows the calorimetric energy per hit for different current configurations. The peak values are around 0.02 GeV per hit on average. Data and simulation show a good agreement in this quantity.
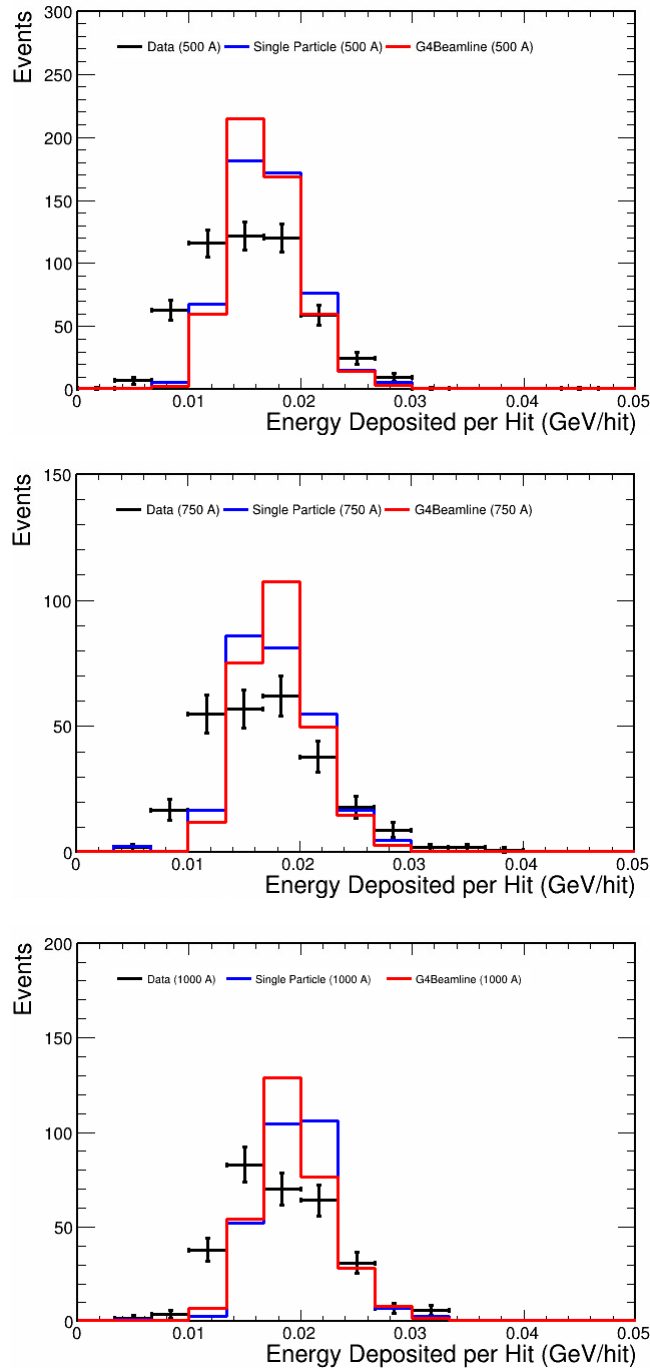
Figure 4.16: Calorimetric energy per hit obtained from data and simulation for different current configurations.

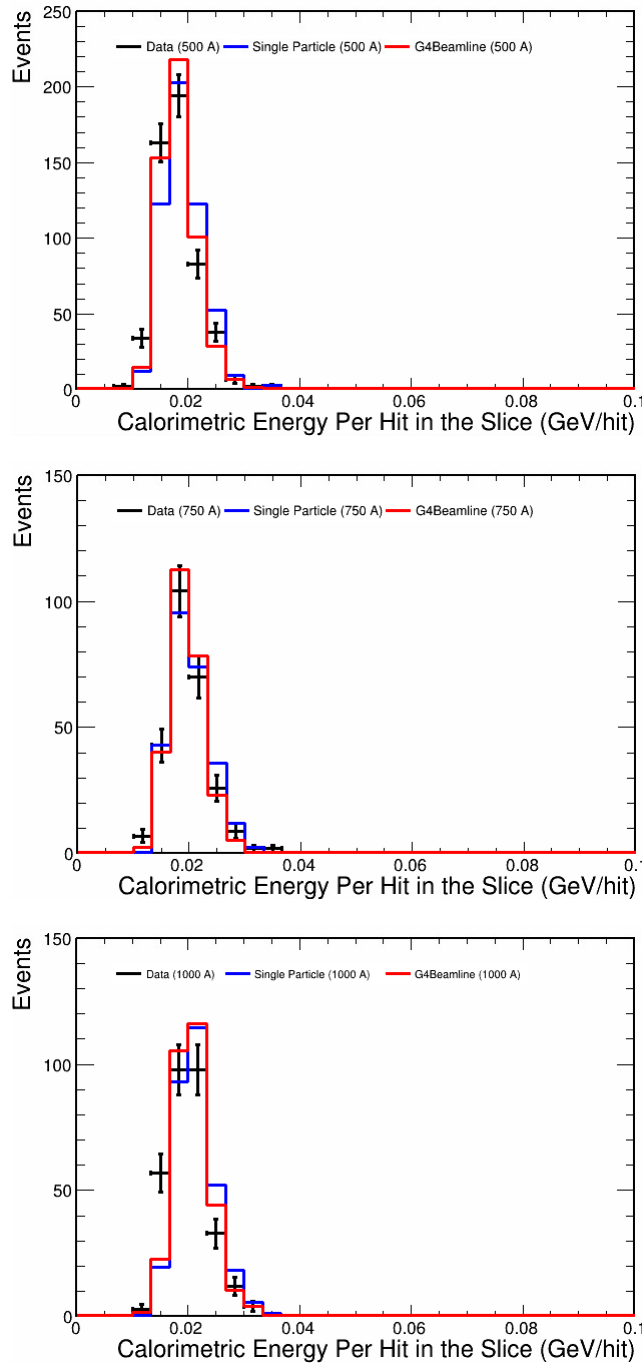- **Calorimetric Energy Per Hit in the Slice**: Figure 4.17 shows the calorimetric energy per hit in the slice for different current configurations. The peak values are around 0.02 GeV per hit on average. Data and simulation show a good agreement in this quantity.

Figure 4.17: Calorimetric energy per hit in the slice obtained from data and simulation for different current configurations.

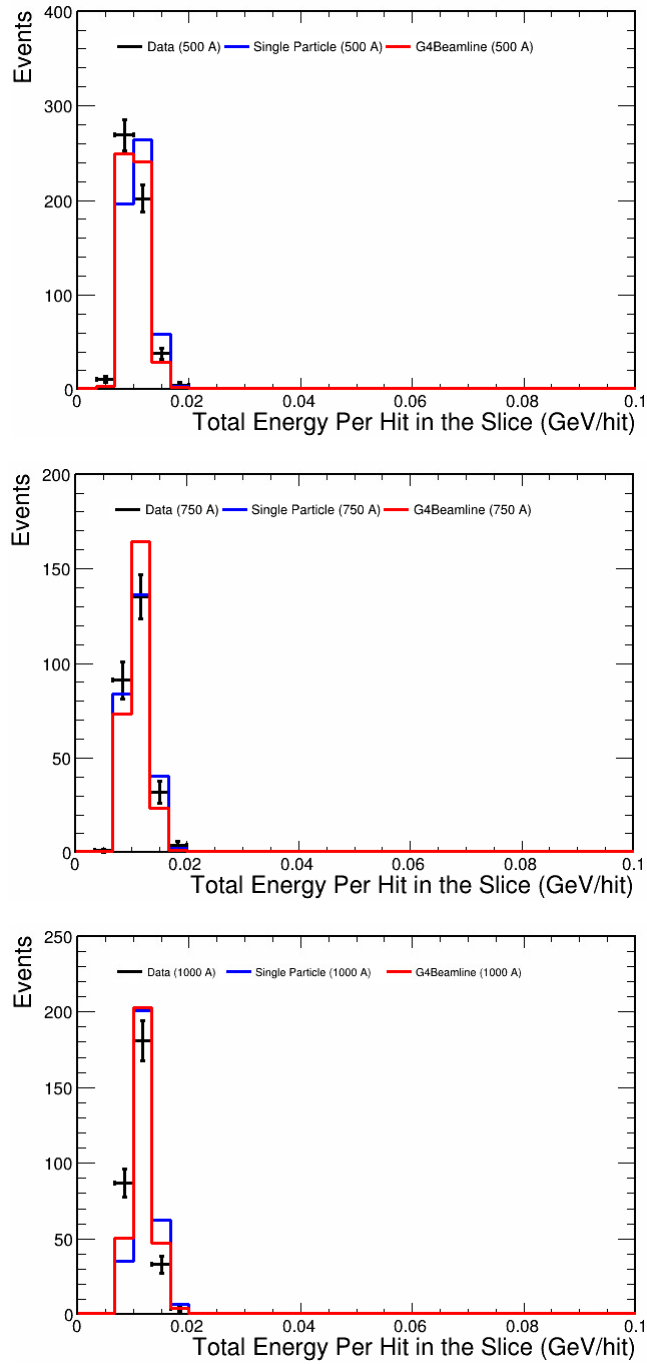- **Total Energy Per Hit in the Slice**: Figure 4.18 shows the total energy per hit in the slice for different current configurations. The peak values are around 0.011 GeV per hit on average. Data and simulation show a good agreement in this quantity.

Figure 4.18: Total energy per hit in the slice obtained from data and simulation for different current configurations.

- **Angular Distribution with Respect to X-Axis**: Figure 4.19 shows the angular distribution of the electrons with respect to the X-axis. The plots show that the electrons enter the detector at a right angle with respect to the X-axis of the detector. Results obtained from data and simulation agree well.
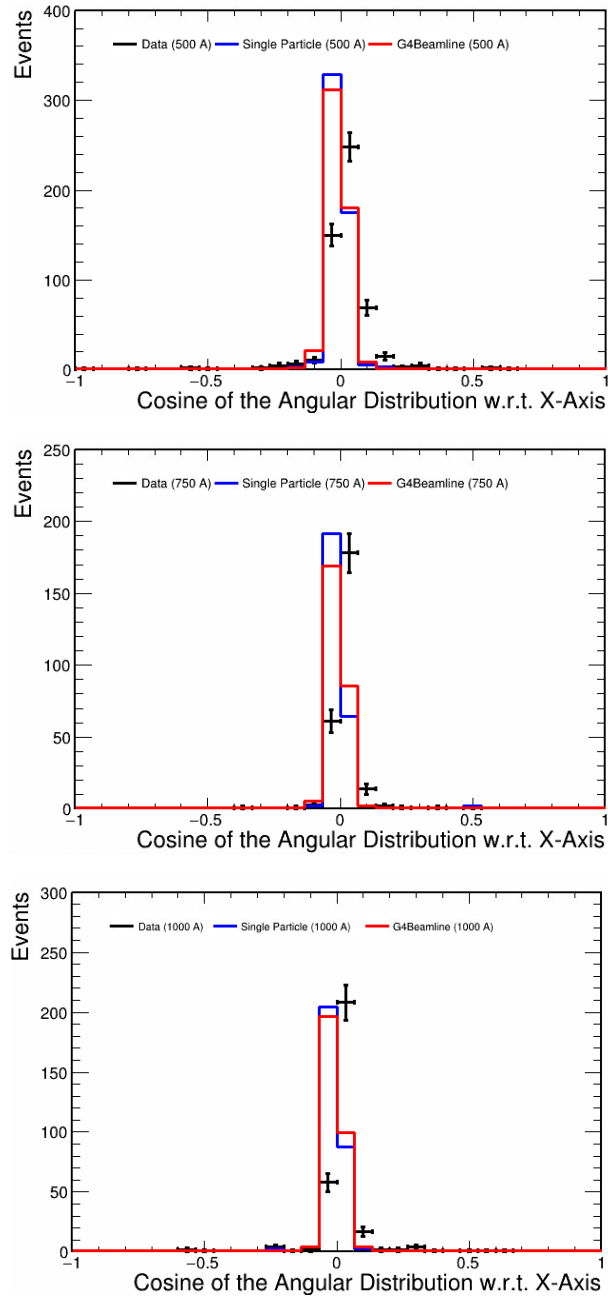
Figure 4.19: Angular distribution of the electrons with respect to X-axis obtained from data and simulation for different current configurations.

- **Angular Distribution with Respect to Y-Axis**: Figure 4.20 shows the angular distribution of the electrons with respect to the Y-axis. The plots show that the electrons enter the detector at a right angle with respect to the Y-axis of the detector. Results obtained from data and simulation agree well.
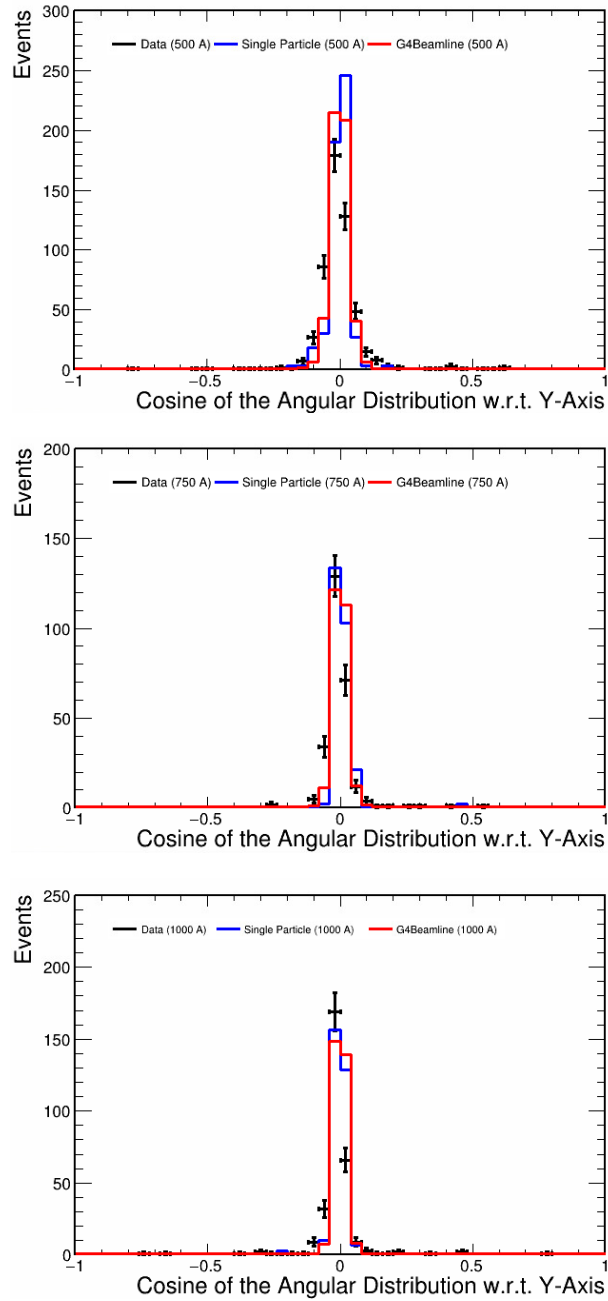
Figure 4.20: Angular distribution of the electrons with respect to Y-axis obtained from data and simulation for different current configurations.

- **Angular Distribution with Respect to Z-Axis**: Figure 4.21 shows the angular distribution of the electrons with respect to the Z-axis. The plots show that the electrons enter the detector along the Z-axis of the detector which is also the direction of the incoming beam. Results obtained from data and simulation agree well.
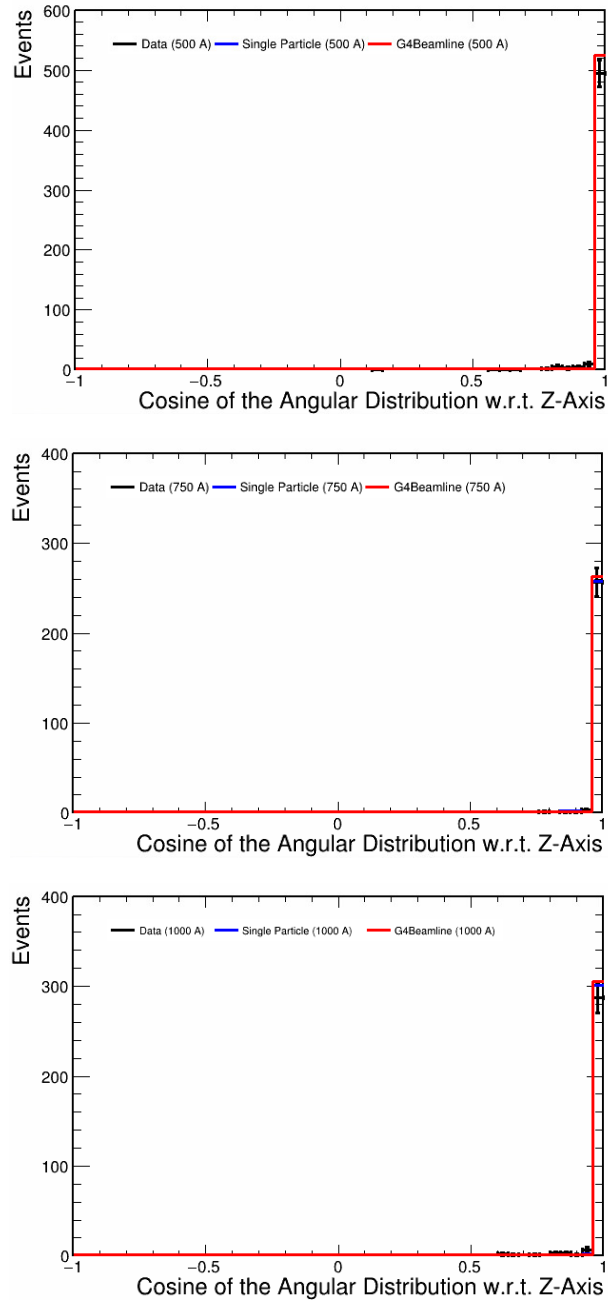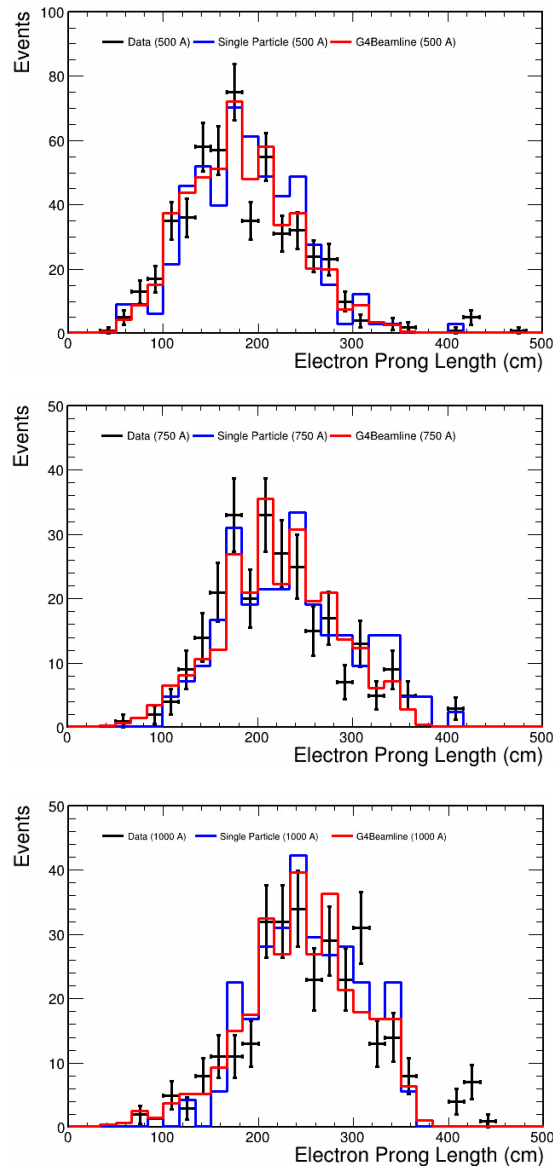

Figure 4.21: Angular distribution of the electrons with respect to Z-axis obtained from data and simulation for different current configurations.

- **Electron Prong Length**: Figure 4.22 shows the plots of electron prong length obtained from data and simulation. The peak values of electron prong length differ according to different current configurations. As the electrons gain momentum, they traverse further along the detector. A length cut around 380 cm has been applied in the plots below to exclude any muons traversing along the detector (Figure 4.23). Results obtained from data and simulation agree well.

Figure 4.22: Electron prong length obtained from data and simulation for different current configurations.
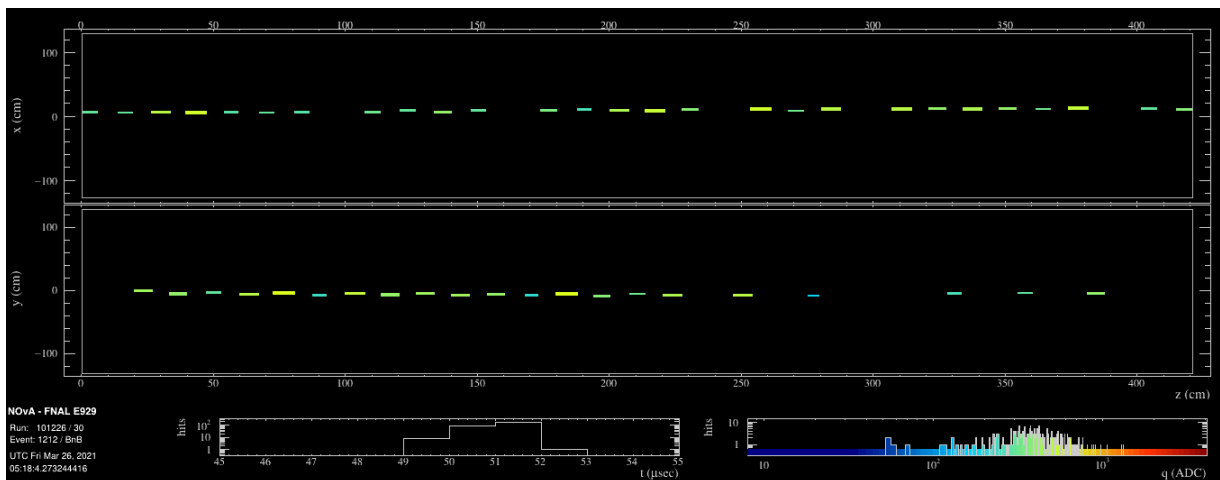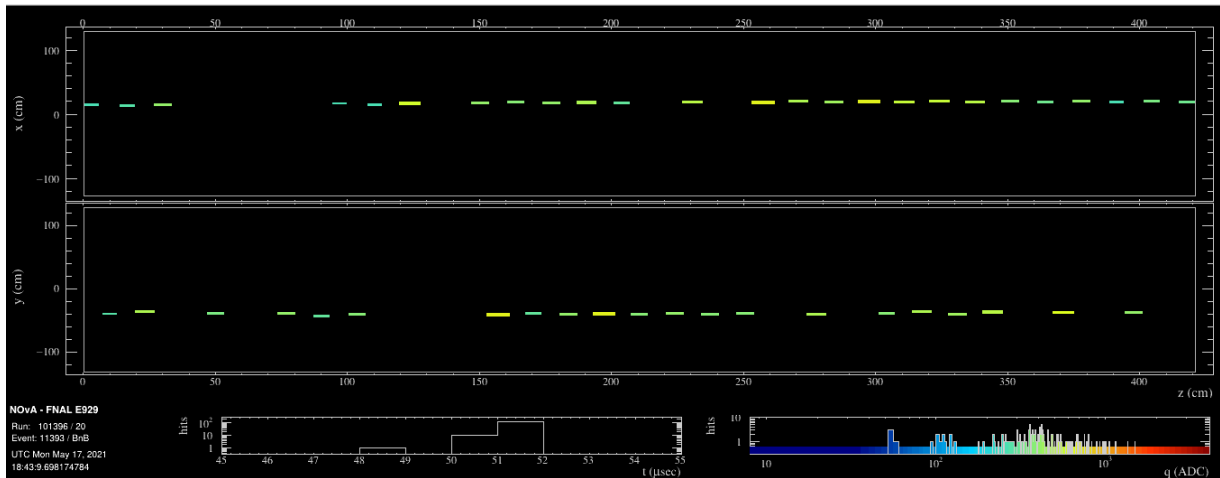
Figure 4.23: The electron sample is contaminated by muons as shown in the event displays. A length cut around 380 cm is applied to exlude these muons in the electron sample.

- **Start Position of Prong in X Direction**: Figure 4.24 shows the start position of prong in X direction. The plots show that the start position of prong in X direction is around -20 cm to 20 cm for all current configurations. The results obtained from data and simulation agree well.
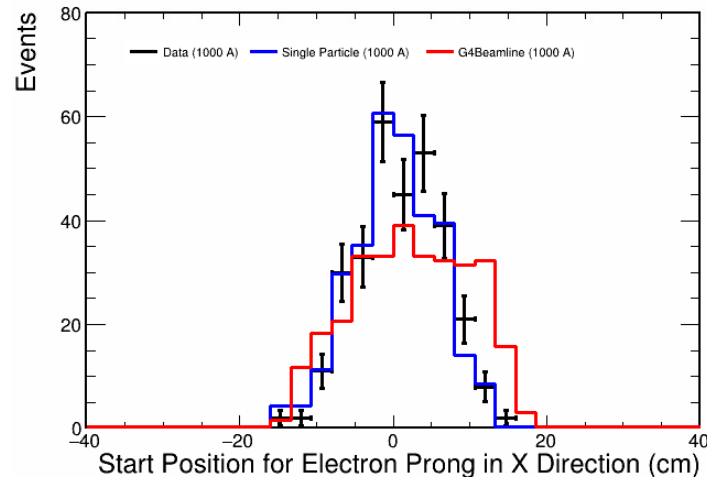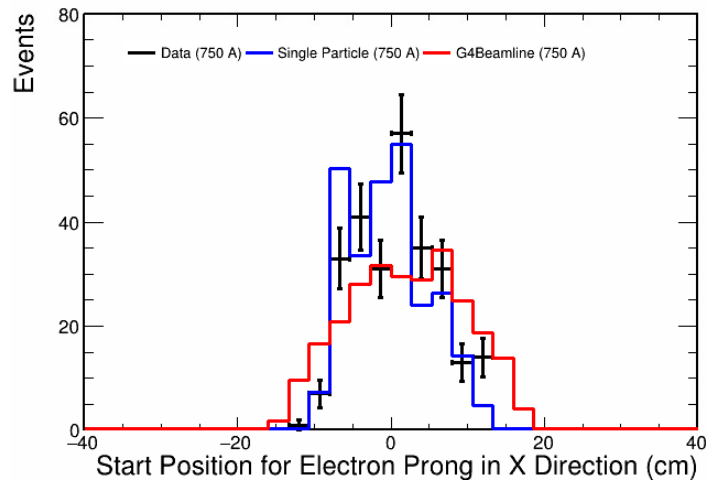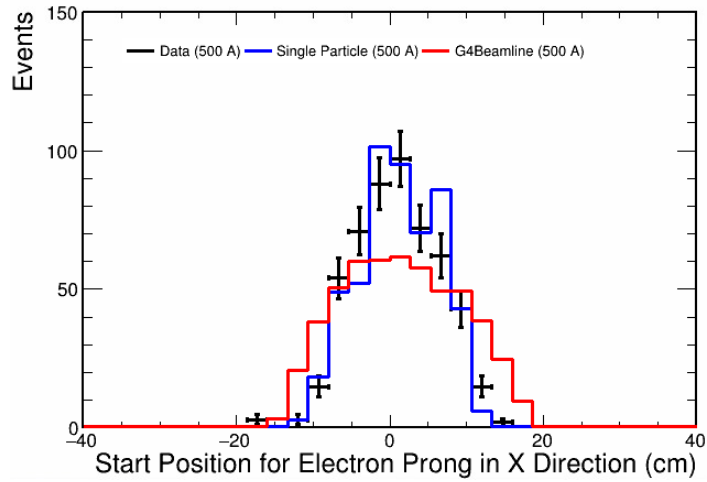
Figure 4.24: Start position of prong in X direction obtained from data and simulation for different current configurations.

- **Start Position of Prong in Y Direction**: Figure 4.25 shows the start position of prong in Y direction. The plots show that the start position of prong in Y direction is around -20 cm to 0 cm for all current configurations. The results obtained from data and simulation agree well.
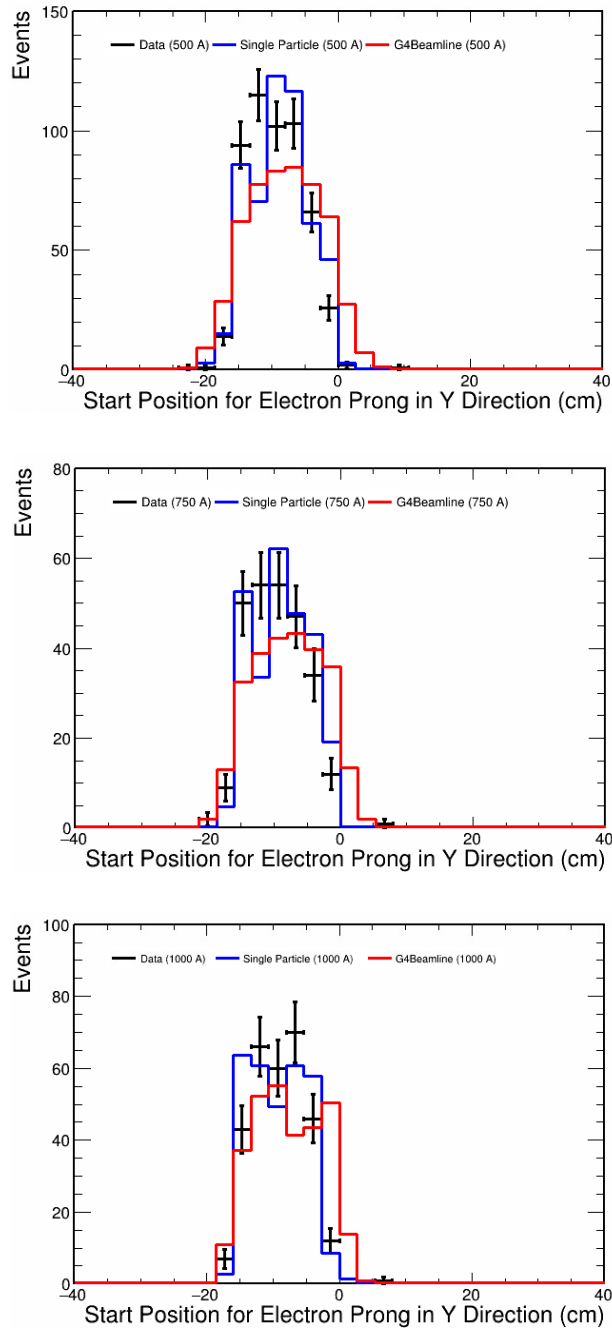
Figure 4.25: Start position of prong in Y direction obtained from data and simulation for different current configurations.

- **Start Position of Prong in Z Direction**: Figure 4.26 shows the start positions of prong in Z direction. Three distinct peaks are seen in the start position of prongs in the Z direction around 4 cm, 10 cm and 18 cm respectively. This is because some of the electrons miss the first plane and deposit hits in the subsequent planes. The results obtained from data and simulation agree well.

Figure 4.26: Start position of prong in Z direction obtained from data and simulation for different current configurations.

Given the time constraint for thesis preparation, further investigation on the source of discrepancy between data and simulation was not possible. Studies with a new calibration will be performed in a near future. This analysis serves as a good reference for future studies on electron energy response measurement which is already underway within the NOvA Test Beam group.

4.3 Fake Data Study of the Effect of Reduced Systematics on the Measurement of Neutrino Oscillation Parameters
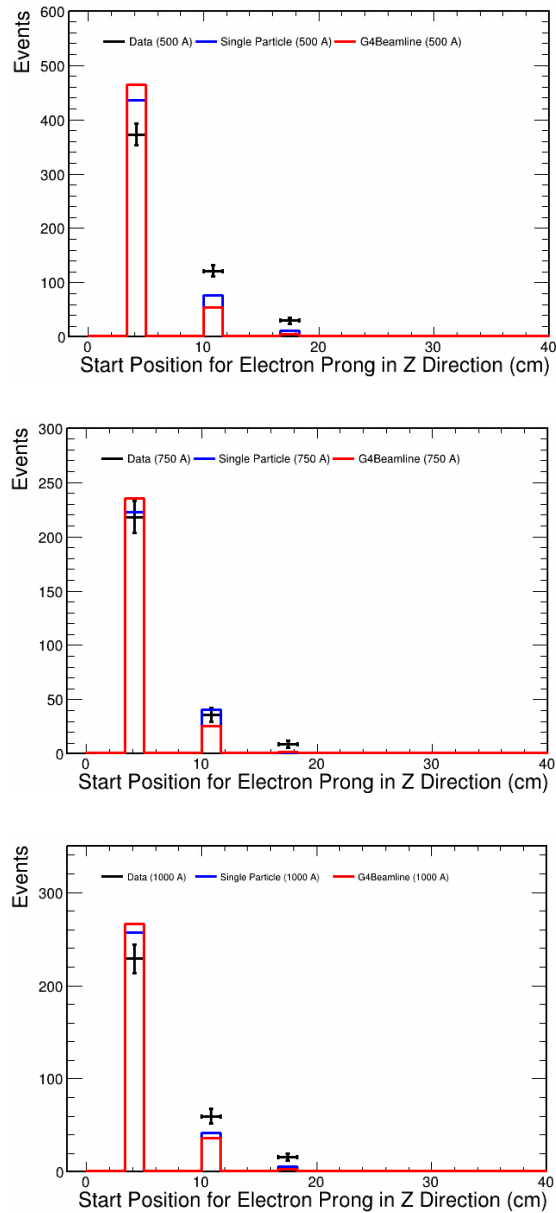
As discussed in the earlier section, the Test Beam experiment was established to address the systematic uncertainties associated with the measurement of neutrino oscillation parameters. The goal of the Test Beam experiment is to reduce these uncertainties. Detector calibration is the largest contributor to the systematic uncertainties standing at 5% uncertainty. In this section, a tentative study of the potential effect on the measurement of neutrino oscillation parameters is discussed if the Test Beam experiment were to achieve its goal of reducing the systematic uncertainties.

The latest NOvA results on improved measurements of the neutrino oscillation parameters[17] are presented below in Figure 4.27 for both normal and inverted hierarchies at 90% confidence limit. The area enclosed by the contour represents the region where the probable numeric values of the respective oscillation parameter lies with a dot being the point of best fit. The smaller the area enclosed by the contour, the larger is the accuracy and sensitivity in the measurement of oscillation parameters. With all the systematic ucnertainties included and Feldman-Cousins corrections applied, the best fit for the oscillation parameters are: $\sin^2 \theta_{23} = 0.57^{+0.03}_{-0.04}$, $\triangle m^2_{32} = (+2.41 \pm 0.07) \times 10^{-3}$ eV^2 for Normal Ordering and $\delta_{CP} = 0.82\pi$. The NOvA results disfavored Inverted Ordering by 1σ. The results are consistent with other long-baseline and atmospheric experiments for "atmospheric parameters". There is an ongoing joint fit between T2K experiment and NOvA experiment including all the systematics, the first results of which is soon to be out.
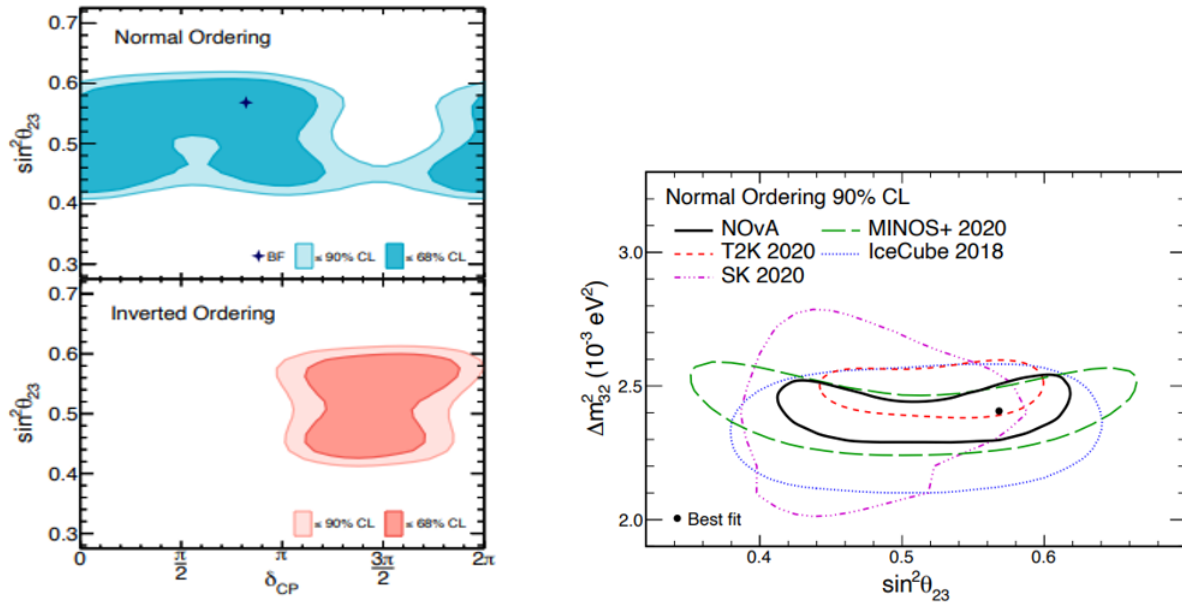
Figure 4.27: Results from the latest measurements of neutrino oscillation parameters.

An ideal case scenario of the measurements of neutrino oscillation parameters without the uncertainty arising from detector calibration is presented through a fake data study. The results are presented and compared with the real-world case of uncertainty from the detector calibration in Figure 4.28 and Figure 4.29.
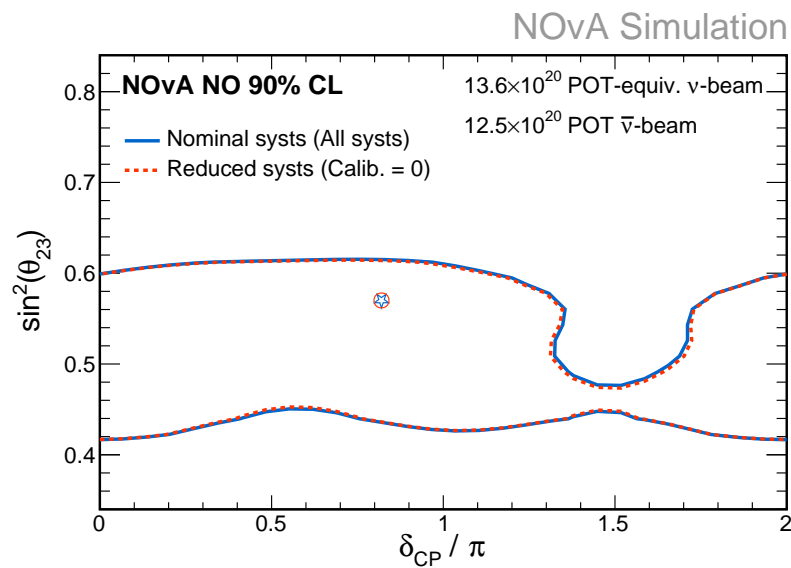
Figure 4.28: Fake data study of the impact of no calibration systematic on the plot of $\sin^2\theta_{23}$ vs δ_{CP}.
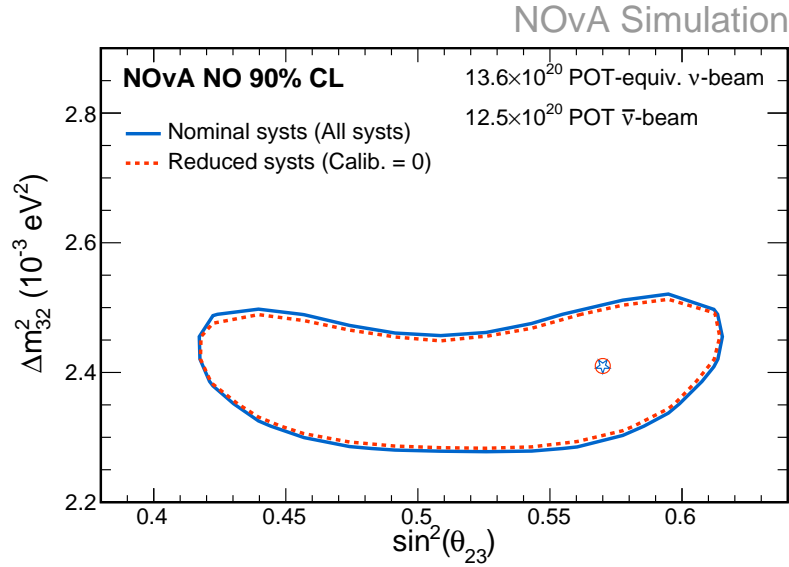
Figure 4.29: Fake data study of the impact of no calibration systematic on the plot of $\triangle m^2_{32}$ vs $\sin^2\theta_{23}$.

The above diagrams show that the measurement of neutrino oscillation parameters would be affected if there were to be an ideal case scenario without the uncertainty arising from detector calibration. Fake data study shows that the area enclosed would decrease if the systematics due to detector calibration were absent, thereby increasing the accuracy and in the measurement of the oscillation parameters' value.

This study suggests that the sensitivity in measuring the oscillation parameters' value would increase in absence of the systematics due to detector calibration. It also hints that there's more to understand about the implications of calibration uncertainty. If detector calibration is the leading source of systematic uncertainty, getting rid of it should have more effect on the measurement of the oscillation parameters. Further studies on the impacts of systematics on the measurements of oscillation parameters can be performed to extrapolate meaningful information.

CHAPTER 5

CONCLUSION

This thesis explains the theory of neutrino oscillation in detail and describes the way NOvA experiment is designed to measure the neutrino oscillation parameters. The analysis done for this thesis addresses the systematic uncertainties associated with the measurement of neutrino oscillation parameters. The ultimate goal of this analysis is to reduce the systematic uncertainties to improve the measurement of neutrino oscillation parameters such as $\triangle m^2_{32}$, δ_{CP} and $\sin^2(\theta_{23})$. The analysis also aims to validate the detector response through Test Beam data and simulation.

While Chapter 1 touches base on the introduction and importance of the Standard Model, neutrinos and neutrino oscillations in general, chapter 2 focuses on how NOvA eperiment measures the neutrino oscillation parameters. Data Quality plays a significant role to select good and accurate data for 3-flavor analysis. The Data Quality plots are also constantly being monitored by the shifters to inspect the detector performance.

In chapter 3, the introduction and motivation behind the Test Beam program are summarized. The conclusion of Test Beam electron analysis in chapter 4 hints that while there are no apparent discrepancies in other electronic properties, calibration could be the biggest factor for significant discrepancy between data and simulation results seen in the energy variables. Further studies are required to validate calibration which are currently underway within the Test Beam group. Fake data study of the effect of reduced calibration systematic hinted at increased accuracy in measuring the oscillation parameters. It is also equally essential to perform studies to validate the reconstruction and simulation in Test Beam in order to understand the actual source of discrepancy. With further studies on validation, the detector response can then be comprehended with more certainty.

Once the detector response is validated, further digging can be done into the sources of detector calibration uncertainty. As NOvA makes use of simulation in calibration, the detector

calibration is the biggest contributor to systematic uncertainties with 5% uncertainty. Further studies on validation and energy deposition from well-characterized charged particles will enable Test Beam to understand the detector calibration. This will then reduce the systematic uncertainties and lead to accurate measurements of the neutrino oscillation parameters.

LIST OF REFERENCES

1. I.C. Bainau *et al*. *Fundamentals of Physics and Nuclear Physics*. 2009.

2. URL `https://web.archive.org/web/20180911042958/https:/home.cern/topics/antimatter`.

3. S. Weinberg. *The Quantum Theory of Fields*. Cambridge University Press, Cambridge, 1995.

4. D. Griffiths. *Introduction to Elementary Particles*. Wiley-VCH, Weinheim, Germany, 2nd edition, 2008.

5. P. Huber *et. al.* Snowmass Neutrino Frontier Report, 2022.

6. R. Oerter. *The Theory of Almost Everything: The Standard Model, the Unsung Triumph of Modern Physics*. Penguin Group, New York, 2006. ISBN 978-0-13-236678-6.

7. S. Carroll, Z. Rhoades, and J. Leven. *Dark Matter, Dark Energy: The Dark Side of the Universe*. The Teaching Company, Chantilly, VA, 2007. ISBN 978-1-59803-350-2.

8. D. Perkins. *Introduction to High Energy Physics*. Cambridge University Press, 4th edition, 2014.

9. P. Lipari. Introduction to Neutrino Physics, 2009. URL `https://cds.cern.ch/record/677618/files/p115.pdf`.

10. J. J. Sakurai and J. J. Napolitano. *Modern Quantum Mechanics*. Pearson, 2nd edition, 2011.

11. B. Pontecorvo. Inverse Beta Processes and Nonconservation of Lepton Charge. *Sov. Phys. JETP*, 7:172–173, 1958.

12. Z. Maki, M. Nakagawa, and S. Sakata. Remarks on the Unified Model of Elementary Particles. *Progress of Theoretical Physics*, 28(5):870–880, 1962.

13. B. Pontecorvo. Neutrino Experiments and the Problem of Conservation of Leptonic Charge. *Sov. Phys. JETP*, 26:984–988, 1968.

14. H. Harari and M. Leurer. Recommending a Standard Choice of Cabibbo Angles and KM Phases for Any Number of Generations. *Phys. Lett. B*, 181:123–128, 1986.

15. N. Cabibbo. Time Reversal Violation in Neutrino Oscillation. *Phys. Lett.*, 72B:333–335, 1978.

16. M.A. Acero *et al*. Search for Multimessenger Signals in NOvA Coincident with LIGO/Virgo Detections. *Physical Review D*, 101(11), 2020. doi: 10.1103/physrevd.101.112006.

17. M.A. Acero *et al*. Improved Measurement of Neutrino Oscillation Parameters by the NOvA Experiment. *Phys. Rev. D*, 106:032004, 2022. doi: 10.1103/PhysRevD.106.032004.

18. A. Dombara. *Constraining Beam Backgrounds and Analyzing the Detector Response in a Test Beam with the NOvA Experiment*. PhD thesis, Syracuse University, 2022.

19. P. Adamson *et al.* The NuMI Neutrino Beam. *Nuclear Instruments and Methods in Physics Research*, 806:279–306, 2016. doi: 10.1016/j.nima.2015.08.063.

20. A. Sousa, R. Nichol, and J. Nelson. Draft of Test Beam Task Force Report. NOvA Internal Document (DocDB-15750), 2016.

21. T. Lackey. *Proton Scattering in NOvA Test Beam*. PhD thesis, Indiana University, 2022.

22. S. Agostinelli *et al.* GEANT4 - A Simulation Toolkit. *Nuclear Instruments and Methods in Physics Research*, 506:250, 2003. doi: 10.1016/S0168-9002(03)01368-8.

23. URL `https://cdcvs.fnal.gov/redmine/projects/novatestbeam/wiki`.

24. A. Dombara. Test Beam Run-3 Data. NOvA Internal Document (DocDB-50211), 2021.

25. M. Wallbank. Introduction to NOvA Test Beam Analyses. NOvA Internal Document, 2021.

VITA

DEVESH BHATTARAI

EDUCATION

Master's of Science in Physics   July 2023
The University of Mississippi
Oxford, Mississippi, USA

Bachelor's of Science in Physics   October 2017
Tribhuvan University
Kirtipur, Kathmandu, Nepal

EXPERIENCE

Teaching Assistant   August 2019 - May 2023
The University of Mississippi

Research Assistant   Summer 2020, 2021, 2022, 2023
The University of Mississippi

Good Runs Expert   January 2021 - December 2022
NOvA Data Quality

Detector and Systematics Monitoring   December 2020 - March 2023
NOvA Experiment

Data Analysis of Test Beam Electrons   June 2021 - July 2023
NOvA Test Beam

PROJECTS

NOvA Data Quality   January 2012 - December 2022
NOvA Experiment

NOvA Test Beam   June 2021 - July 2023
NOvA Experiment

SELECTED PUBLICATIONS

[1] Acero, M.A. *et. al.* (August 2022). Improved Measurement of Neutrino Oscillation Parameters by the NOvA Experiment. *Phys. Rev. D* 106, 032004, (032004 1 - 032004 12). **DOI**: 10.1103/PhysRevD.106.032004

[2] Acero, M.A. *et. al.* (February 2023). Measurement of the ν_e - Nucleus Charged-Current Double-Differential Cross Section at $< E_\nu >= 2.4$ GeV Using NOvA. *Phys. Rev. Lett.* 130, 051802, (051802 1 - 051802 7). **DOI**: 10.1103/PhysRevLett.130.051802

[3] Acero, M.A. *et. al.* (March 2023). Measurement of the Double-Differential Muon-neutrino Charged-Current Inclusive Cross Section in the NOvA Near Detector. *Phys. Rev. D* 107, 052011, (052011 1 - 052011 20). **DOI**: 10.1103/PhysRevD.107.052011

SELECTED CONFERENCE PRESENTATIONS

Talk Title: The Data Quality at the NOvA Experiment
American Physical Society (APS) Annual April Meeting   April 2022
New York City, New York, USA

Poster Title: Measuring Electromagnetic Activity with the NOvA Test Beam
American Physical Society (APS) Annual April Meeting   April 2022
New York City, New York, USA

Talk Title: Electron Energy Response Measurement in the NOvA Test Beam Detector
89th Annual Meeting of the Southeastern Section of the APS (SESAPS)   November 2022
The University of Mississippi
Oxford, Mississippi, USA

AWARDS

Graduate Research Assistantship   Summer 2020, 2021, 2023
Awarder: Assistant Prof. Dr. Gavin Davies

Graduate Research Assistantship Summer 2022

Awarder: Department of Physics and Astronomy, The University of Mississippi

Conference Travel Grant April 2022

Awarder: Department of Physics and Astronomy, The University of Mississippi

Conference Travel Grant April 2022

Awarder: Graduate School, The University of Mississippi